RESEARCH ARTICLE

Brain
Pathology

Accumulation of misfolded SOD1 outlines distinct patterns of motor neuron pathology and death during disease progression in a SOD1^{G93A} mouse model of amyotrophic lateral sclerosis

Sara Salvany | Anna Casanovas | Lídia Piedrafita | Sílvia Gras | Jordi Calderó | Josep E. Esquerda 🄳

Patologia Neuromuscular Experimental, Departament de Medicina Experimental, Facultat de Medicina, Universitat de Lleida and Institut de Recerca Biomèdica de Lleida (IRBLleida), Lleida, Catalonia, Spain

Correspondence
Josep E. Esquerda, Departament de Medicina Experimental, Facultat de Medicina, Universitat de Lleida-IRBLleida, Av. Rovira Roure 80, 25198 Lleida, Spain.
Email: josep.esquerda@udl.cat

Abstract

Early misfolded superoxide dismutase 1 (mfSOD1) accumulation, motor neuron (MN) degeneration, and microgliosis are hallmark pathological features in SOD1^{G93A} amyotrophic lateral sclerosis (ALS) mice. Because of the different vulnerabilities of distinct MN subtypes, degenerating and surviving MNs coexist in different proportions during disease progression. By examining the expression of misfolded conformers of SOD1 using specific antibodies, we defined distinct MN phenotypes that were evaluated during disease progression and the local neuroinflammatory reaction. The most severe phenotype corresponded to somata of fast-twitch subtype MNs, which exhibited highly positive mfSOD1 immunostaining and an extreme degree of vacuolar degeneration. Vacuoles, which are of mitochondrial origin, contain mfSOD1 in conjunction with nonmitochondrial proteins, such as chromogranin, CD81, and flotillin. The fusion of ER-derived vesicles enriched in mfSOD1 with outer mitochondrial membranes is thought to be the primary mechanism for vacuole formation. In addition, the ulterior coalescence of enlarged mitochondria may lead to the formation of giant vacuoles. Vacuolar degeneration is a transient degenerative process occurring early during the presymptomatic stages of the disease in ALS mice. Some vacuolated MNs are also positive for pMLKL, the effector protein of necroptosis. This indicates a newly described mechanism in which extracellular vesicles derived from damaged MNs, via cellular secretion or necroptotic disruption, may be the triggers for initiating neuroinflammation, glial-mediated neurotoxicity, and disease spreading. Furthermore, as MN degeneration in mutant SOD1 mice is noncell autonomous, the effects of experimentally increasing or decreasing the microglial response on the expression of MN phenotypes were also evaluated, demonstrating bidirectional cross talk signaling between the degree of expression of mfSOD1 and local neuroinflammation. More detailed knowledge regarding these processes occurring long before the end stages of the disease is necessary to identify novel molecular targets for future preclinical testing.

KEYWORDS
amyotrophic lateral sclerosis, microglia, motor neuron, necroptosis, SOD1, vacuolar degeneration

Jordi Calderó and Josep E. Esquerda senior co-authors.

----

1 | INTRODUCTION

Amyotrophic lateral sclerosis (ALS) is a fatal degenerative disease primarily involving the spinal cord and brain motor neurons (MNs), leaving muscles denervated [1]. Most ALS cases are sporadic, while 10% are familial, and among them, 20% have been linked to mutations in the superoxide dismutase 1 (SOD1) gene [2]. Rather than via a loss of function, mutant SOD1 determines the ALS phenotype via a gain of neurotoxic properties, which includes oxidative stress, protein aggregation, mitochondrial dysfunction, and neuroinflammation [3]. The SOD1^{G93A} ALS mouse model overexpresses ∼25 copies of the human gene encoding the enzyme SOD1 carrying a mutation that causes familial ALS. Since its development in 1994, this model has been extensively used to investigate the pathogenic mechanisms leading to ALS because it recapitulates many phenotypic features observed in ALS patients [4–8].

SOD1^{G93A} mice exhibit progressive paralysis starting at ∼90 days, with death occurring at ∼135 days, depending on the genetic background. In this mutant mouse model, the decrease in motor function occurs concomitantly with the development of conspicuous and severe pathological changes that include the loss of α-MN and reactive astrocytosis and microgliosis. MN pathology and dysfunction progress with notable temporal reproducibility, a condition that is essential for the correlation of data from individuals of different ages in longitudinal studies. This has led to the demarcation of presymptomatic (P30–P90), symptomatic (P90–P120), and end-stage (P120 to death) periods in the time course of the disease as a reference in many experimental studies [8–10]. One intriguing aspect of ALS pathology is the distinct degrees of vulnerability among the different MN groups or subtypes; for example, fast-twitch, fast-fatigable MNs are severely affected and degenerate first, while slow-twitch MNs are less vulnerable to ALS [11–13]. In addition, MNs that innervate extraocular muscles or external sphincters are considered ALS resistant (reviewed in [12,14]). Low MN excitability is correlated with ALS resistance [15], and γ-MNs, which innervate muscle spindles, are entirely spared from ALS pathology [16]. After early loss of the most vulnerable MNs, axons of the remaining MNs sprout to compensate for those that have degenerated [17]. This means that, at a given time, degenerating and surviving (perhaps regenerating) MNs coexist at the spinal cord ventral horn in variable proportions during disease progression. Thus, the corresponding pathomorphological status of individual MNs should be heterogeneous and dissociated from the clinical outcome of the disease. For example, severely damaged MNs could be present (although in a minor proportion) at the early stages and vice versa, and some apparently healthy MNs would be present at the end-stage period. Given our limited knowledge regarding the sequence of cellular events that occur during disease progression, we attempted to categorize ALS MN pathology at the single-cell level by establishing distinct phenotypic patterns of damage based on the expression of toxic forms of misfolded SOD1 (mfSOD1). MN degeneration in mutant SOD1 mouse models is noncell-autonomous, and the participation of adjacent cells appears to be essential for disease pathogenesis [18–20]. For this reason, the examination of MN neuropils, including afferent synapses, astrocytes, and microglia, in relation to defined cell body phenotypes was included in our analysis. A better characterization of how degenerative and reactive changes are spatially and temporally distributed will help to determine the effects of putative therapeutic agents in preclinical assays in the SOD1^{G93A} fast mouse model of ALS. In addition, it seems that before NM degeneration, a process of a motor axon dying back determines an early disconnection of MNs from their muscle targets [11,21]. The interruption of nerve-muscle interactions also occurs in healthy animals after peripheral nerve transection (axotomy), resulting in a CNS response that includes glial activation around axotomized MNs and a loss of synaptic afferents contacting MN cell bodies [22–24]. Thus, the reactive response observed in axotomized MNs may share some common pathogenic mechanisms with ALS. However, in contrast to what occurs in ALS, MN cell body activation in response to peripheral nerve axotomy in adults is not usually followed by MN death [25,26]. Instead, axotomy triggers the expression of "regeneration-associated genes", shifting neurons from "transmitting" to a "growth" mode, which provides MNs with the structural and molecular machinery for restoration of neuromuscular connectivity [22]. Although it may be deleterious in some respects [24,27], the glial neuroinflammatory response in the vicinity of axotomized MNs is also considered neuroprotective [28,29]. Therefore, analyzing afferent synapses and the glial response in axotomized MNs in WT and mutant SOD1 genetic backgrounds may provide new clues for understanding the mechanisms of MN degeneration in ALS.

2 | MATERIAL AND METHODS

2.1 | Animals, surgical procedures, and pharmacological treatments

SOD1^{G93A} (B6SJL-Tg[SOD1-G93A]1Gur/J) mice were purchased from Jackson Laboratory (Sacramento, CA, USA) and maintained as hemizygotes by breeding transgenic males with B6SJL females. Transgenic progeny was identified by PCR genotyping of DNA extracted from the tail using specific primers as previously described [30]. Age-matched wild-type (WT) littermates of transgenic animals were used as controls. Briefly, asymptomatic mice were considered at postnatal day (P) 0–P30, presymptomatic at P30–P60, symptomatic at P60–P90, and in end-stage at P90–

P120 $\pm$ 10 [31]. Previously described endpoint criteria were used to minimize suffering [32]. To avoid potential bias because of gender, only male animals were used in this study. Mice were housed 5–6 per cage with ad libitum access to standard laboratory chow and water under a 12-h light/dark cycle. According to previously defined criteria [33], mice displaying tumors or physical abnormalities were excluded from the study and euthanized by an overdose of pentobarbital (30 mg, intraperitoneally [i.p.]). All efforts were made to reduce the number of animals used in agreement with the European Communities Council Directive (24 November 1986, 86/609/EEC).

All animal experimentation procedures were performed according to the European Committee Council Directive and the norms established by the Generalitat de Catalunya (published as a law in the *Diari Oficial de la Generalitat de Catalunya* 2073, 1995). All experiments were previously evaluated and approved by the Committee for Animal Care and Use of our University of Lleida.

For axotomy experiments in young and adult (P30, P60, and P90) mice, the unilateral sciatic nerve was transected and ligated at the femoral level in the proximal stump to prevent spontaneous reinnervation. Animals were anesthetized with a combination of ketamine (100 mg/kg) and xylazine (10 mg/kg) and maintained with inhalant anesthesia (1% isoflurane). To minimize suffering, mice were administered postoperative analgesia with subcutaneously injected buprenorphine (0.05 mg/kg). Lumbar spinal cord samples were obtained 7 days after axotomy.

For pharmacological approaches, adult mice (P60) were used. Drug delivery regimes were based on published reports (Saxena et al.), and the delivery protocols were as follows: methoctramine (Sigma-Aldrich) as a daily dose for 15 days administered i.p. in saline at 200 µg/kg; oxotremorine M (Tocris Bioscience) as a daily dose for 15 days administered i.p. in saline at 30–50 µg/kg.

The colony-stimulating factor 1 receptor (CSF-1R)-specific kinase inhibitor (PLX5622) [34] was generously provided by Plexxikon Inc. and formulated in AIN-76 standard chow by Research Diets Inc. One-month-old male mice were housed in a specific pathogen-free environment and treated with 1.200 mg/kg PLX5622 in chow for 30 days. To verify PLX5622 consumption by the mice, their weight was monitored; no significant weight reduction was observed.

2.2 | Tissue sample preparation, histological analysis, and motoneuron counts

Mice were deeply anesthetized and transcardially perfused with physiological saline solution, followed by 4% paraformaldehyde (PFA) in 0.1-M phosphate buffer (PB) pH 7.4; lumbar spinal cord samples were dissected, postfixed for 24 h at 4°C in the same fixative solution and then transferred to 30% sucrose in 0.1-M PB

containing 0.02% sodium azide for cryoprotection. Transverse cryostat sections (16 µm thick) were collected on gelatine-coated glass slides.

For MN counts, several random cryostat sections representing the lumbar spinal cord segments (L1–L5) were chosen and stained with Cresyl Violet. α-MNs, located in the ventral horn, were identified by their size (soma diameter >20 µm), morphology (multipolar appearance, prominent nucleolus, and abundant Nissl granules in cytoplasm), and topography (Rexed's lamina IX). MNs were blindly quantified on one side of every second section, according to previously described criteria (Calderó et al.) [35]. Briefly, only MNs with a large nucleus, a visible clump of nuclear material, and a substantial intense basophilic cytoplasm were included for quantification. These stringent criteria do not necessarily require the use of a correction factor for double counting. MNs presenting either massive vacuolization or homogeneous dark staining were considered degenerating cells.

2.3 | Immunocytochemistry and imaging

Cryostat sections were permeabilized with phosphate-buffered saline (PBS) containing 0.1% Triton X-100 for 30 min, blocked with either 10% normal goat serum or normal horse serum in PBS for 1 h at room temperature, and then incubated overnight at 4°C with an appropriate primary antibody mixture. The primary antibodies used are listed in Table 1.

After washing with PBS, sections were incubated at room temperature for 1 h with a combination of appropriate secondary fluorescent antibodies labeled with one of the following fluorochromes at a 1/500 dilution: Alexa Fluor 488, DyLight 549, or DyLight 649 (Jackson ImmunoResearch Laboratories). Finally, the spinal cord sections were labeled with blue fluorescent NeuroTrace Nissl staining (1:150; Molecular Probes) and mounted using anti-fading medium containing 0.1 M Tris–HCl buffer (pH 8.5), 20% glycerol, 10% Mowiol, and 0.1% 1,4-diazabicyclo [2,2,2] octane.

The slides were then examined under a FluoView FV-500 or FluoView FV-1000 Olympus laser-scanning confocal microscope (Olympus). MNs were imaged after obtaining optical sections (0.5 or 1 µm) of cell bodies. For comparison, slides from different animals and experimental conditions were processed in parallel for immunocytochemistry and subsequent imaging. The same scanning parameters were used for the acquisition of images corresponding to different experimental groups. Image analysis was performed using FV10-ASW 3.1 Viewer (Olympus) or ImageJ software (US National Institutes of Health).

Immunolabeled profiles of the different protein markers were examined and then manually counted on the screen for each MN soma. The area and perimeter of MN somata and both microglial and astroglial

TABLE 1 Antibodies used for immunocytochemistry

Target	Host species	Source (catalog no.)	Dilution
BiP	Rabbit polyclonal	Abcam (ab21685)	1:1000
C1q	Rabbit monoclonal	Abcam (ab182451)	1:1000
CD68	Rat monoclonal	AbDserotec (MCA1957T)	1:100
CD81	Rabbit polyclonal	Abcam (ab155760)	1:100
Chromogranin-A	Rabbit polyclonal	Santa Cruz (sc-13,090)	1:100
Flotillin	Rabbit polyclonal	Abcam (ab41927)	1:150
Glial fibrillary acidic protein (GFAP)	Chicken polyclonal	Abcam (ab4674)	1:1000
Ionized calcium-binding adaptor molecule 1 (Iba1)	Goat polyclonal	Abcam (ab5076)	1:500
Mac-2	Rat monoclonal	Cedarlane (CL8942AP)	1:800
MLKL (phospho S345)	Rabbit monoclonal	Abcam (ab196436)	1:100 (IF) 1:1000 (WB)
MMP9	Goat polyclonal	Sigma-Aldrich (M9570)	1:10
NRG1 1α /β 1/2	Rabbit polyclonal	Santa Cruz (sc-348)	1:300
P2RY12	Rat monoclonal	BioLegend (848002)	1:100
p62	Rabbit polyclonal	Cell Signaling (#5114)	1:100
PDH	Mouse monoclonal	Abcam (ab110333)	1:1000
PDI	Mouse monoclonal	Enzo Life sciences (ADI-SPA-891)	1:200
SOD1 (AJ10) Anti-Misfolded Human SOD1	Rabbit polyclonal	AbBcn (4251/4252)	1:1000
SOD1 (C4F6) Anti-Misfolded Human SOD1	Mouse monoclonal	MediMabs 2B Scientific (MM-00070-2-P)	1:100
Synaptophysin 1	Guinea pig polyclonal	Synaptic Systems (101004)	1:500
Ubiquitin (P4D1)	Mouse monoclonal	Cell Signaling (#3936)	1:100
Vesicular acetylcholine transporter (VAChT)	Guinea pig polyclonal	Synaptic Systems (139105)	1:500

profiles covering or physically close to MNs were also manually measured (for C1q immunolabeling, the intensity of the labeling was measured and normalized using the intensity of the background). In axotomy experiments, we only analyzed cell bodies located at the Pes9 region of the lumbar 6 spinal cord segment, which corresponds to the sciatic motor column [36]. The pool of axotomized MNs was identified by their close interaction with recruited Iba1-stained microglial cells. The number of synaptic boutons contacting activated microglia in axotomized MNs was evaluated by image analysis (ImageJ).

2.4 | Electron microscopy

Animals were perfused with either 2% PFA or 2% glutaraldehyde in 0.1 M PB (for conventional electron microscopy [EM]) or 4% PFA and 0.1% glutaraldehyde in PB (for ultrastructural immunolabeling). Dissected tissues were postfixed for 24 h at 4°C in the same fixative solution. The samples were sectioned at 200 μm using a vibratome, postfixed in 1% OsO_4 for 2 h, and then contrasted with 0.5% uranyl acetate for 30 min; all procedures were conducted at 4°C. Next, samples were processed for Embed 812 (Electron Microscopy Sciences) epoxy resin, according to standard procedures. Semithin transverse sections (1 μm thick) were stained with Richardson stain and imaged using an Olympus 60×/1.4NA PlanApo oil immersion objective (Olympus) and a DMX 1200 Nikon digital camera. Ultrathin sections were counterstained with Reynold's lead citrate.

For postembedding immunogold analysis, lumbar spinal cords were sectioned at 200 μm using a McIlwain Tissue Chopper (Mickle Laboratory Engineering). After glycerol cryoprotection, samples were rapidly plunged into liquid propane (−184°C) cooled by liquid nitrogen, and processed for freeze substitution using a Leica EM system (Leica Microsystems, Wetzlar, Germany). Tissues were embedded in Lowicryl HM20 resin at low temperature (Electron Microscopy Sciences) following a protocol similar to that described elsewhere [37]. Ultrathin sections were collected using an Ultracut UC6 ultramicrotome (Leica), picked up on formvar-coated nickel grids, washed in PBS and in 50-mM glycine, and then blocked in 5% and 1% bovine serum albumin (BSA). Sections were incubated for 1 h with anti-mfSOD1 protein (C4F6; 1:10) at room temperature. After being rinsed in 0.25 Tween 20, sections were blocked in 1% BSA and incubated in 12 nm gold-conjugated goat anti-mouse IgG (1:30, Sigma-Aldrich), for 30 min at room temperature. After washing in PBS and distilled water, sections were counterstained with uranyl acetate and lead citrate. All observations were performed on a JEOL JEM-1010 transmission electron microscope (Akishima).

2.5 | Western blot

Frozen lumbar spinal cords were fragmented and homogenized using an electric homogenizer (Tissue Grinder) in ice-cold RIPA lysis buffer (50 mM Tris–HCl [pH 7.4], 150 mM NaCl, 1-mM EDTA, 1% NP-40, 1% Na-deoxycholate, 0.1% SDS) supplemented with protease inhibitor (Sigma-Aldrich, cat. # P8340) and PhosSTOP (Roche). Homogenized samples were centrifuged at 13,000 rpm for 20 min at 4°C. The protein concentrations of supernatants were determined by BIO-RAD Micro DC protein assay (BIO-RAD, Laboratories Inc.). Laemmli sample buffer (4×) and 30 μg of protein were loaded in a 10% polyacrylamide electrophoresis gel. Proteins were electrotransferred to polyvinyldifluoride membranes (ImmobilonTM-P, Millipore) in Tris-glycine-methanol-buffered solution. Membranes were blocked in 5% BSA in 0.1% Tween 20 and Tris-buffered saline pH 8 (TBST) for 1 h at RT and then extensively washed in TBST. Immunodetection was performed by incubating the membranes overnight at 4°C with rabbit monoclonal anti-pMLKL (1:1000, Abcam, cat. # ab196436) and mouse monoclonal anti-actin (1:5000, Sigma-Aldrich, cat. # A5441), the latter used for loading controls. Membranes were washed in TBST and incubated with the appropriate peroxidase-conjugated secondary antibodies (1:20,000; Cell Signaling, cat. # 7076) for 60 min at RT, washed in TBST, and visualized using the ECL Prime Western blotting Detection Reagent detection kit (GE Healthcare), as described by the manufacturer. Quantification of band densities was performed using a Chemi-Doc MP Imaging System (BIO-RAD Laboratories Inc.).

2.6 | Statistical analysis

Data are expressed as means $\pm$ SEM. The statistical analysis was assessed and performed using Student's t-test or by one- or two-way analysis of variance (ANOVA), followed by post hoc Bonferroni's test. The level of significance was established at $p < 0.05$. GraphPad Prism 6 software was used for statistical analysis and graphical presentations of data.

3 | RESULTS

3.1 | Three patterns of MN pathology established based on the accumulation of misfolded SOD1[G93A]

The accumulation of mfSOD1 is a hallmark feature of spinal cord pathology in mutant SOD1-mediated ALS animal models. mfSOD1 can be detected by conformational-specific antibodies that are able to distinguish this form of SOD1 from those with a native conformation [38–47]. Because of its neurotoxicity, mfSOD1 is a key element in the pathogenesis of SOD1-mediated familial ALS [48], and it has been suggested that mfSOD1 may play a role in sporadic ALS when wild-type SOD1 adopts a "toxic conformation" through posttranslational modifications [38,42,43,49,50]. Thus, the evaluation of SOD1 expression by means of antibodies such as C4F6 or AJ10 [39,46,47] in individual MNs may provide a valuable readout of their pathologic status [15]. For this purpose, after analyzing mfSOD1 immunostaining, we defined three distinct patterns of its distribution in spinal cord sections in SOD1[G93A] mice, which were categorized as follows (see Figure 1A–H): (i) absence or very low levels of mfSOD1-positive immunoreactivity (phenotype 1); (ii) scattered mfSOD1-positive specks in the ventral horn surrounding MN cell bodies largely devoid of mfSOD1 labeling (phenotype 2); and (iii) MN cell bodies showing highly positive mfSOD1 immunostaining (phenotype 3). Mitochondria have been identified as a primary target of mfSOD1 in the spinal cord [51,52]. Translocation of mutant SOD1 to mitochondria results in swelling and ulterior massive vacuolization, which were widely detected under EM but were also identifiable using light microscopy, particularly in semithin sections [53–55]. As shown in Figure 1B,D,F,H–N and Figure S1, we observed these vacuolated MNs in a pattern that coincides with that described in previous reports [21,56–58]. This type of degeneration allowed us to perform a correlation between the abovementioned mfSOD1-based phenotypes and the cellular structure: (i) in phenotype 1, vacuolar degeneration is scarce or absent; (ii) in phenotype 2, vacuolar degeneration is conspicuous and primarily delimited to MN dendrites and axons; (iii) in phenotype 3, vacuolar degeneration is also extensive within MN somas. EM observations indicated that vacuolar degeneration originated from both massive mitochondrial swelling and endoplasmic reticulum (ER) vesicular fragmentation (Figure 1I–N and Figure S1). The quantitative evaluation of the amount of mfSOD1 immunoreactive deposits in MN cell bodies in relation to the described phenotypes is shown in Figure 2A.

A longitudinal analysis of mfSOD1 during the time course of the disease revealed a gradual decrease of mfSOD1 during its progression from P60 (Figure 2B). The age-related distribution of the three MN phenotypes is shown in Figure 2C; phenotype 2 was highly predominant at P30, whereas phenotype 3 appeared at approximately P60 and extended until the end stages of disease. Most of the phenotype 3 MNs disappeared during a time interval ranging from P90 to end stage, a period in which MN loss reached its maximum concomitantly with MN degeneration (Figure 2D,E). In concordance with phenotype 2, ultrastructural examination at P30 showed mitochondrial vacuolar degeneration restricted to MN processes (dendrites and axons), with only minimal changes detectable in MN somata. These alterations consisted of a focal enlargement of the mitochondrial intermembrane space and early vacuolar changes in the ER (Figure 3A–D). These data are in agreement with those
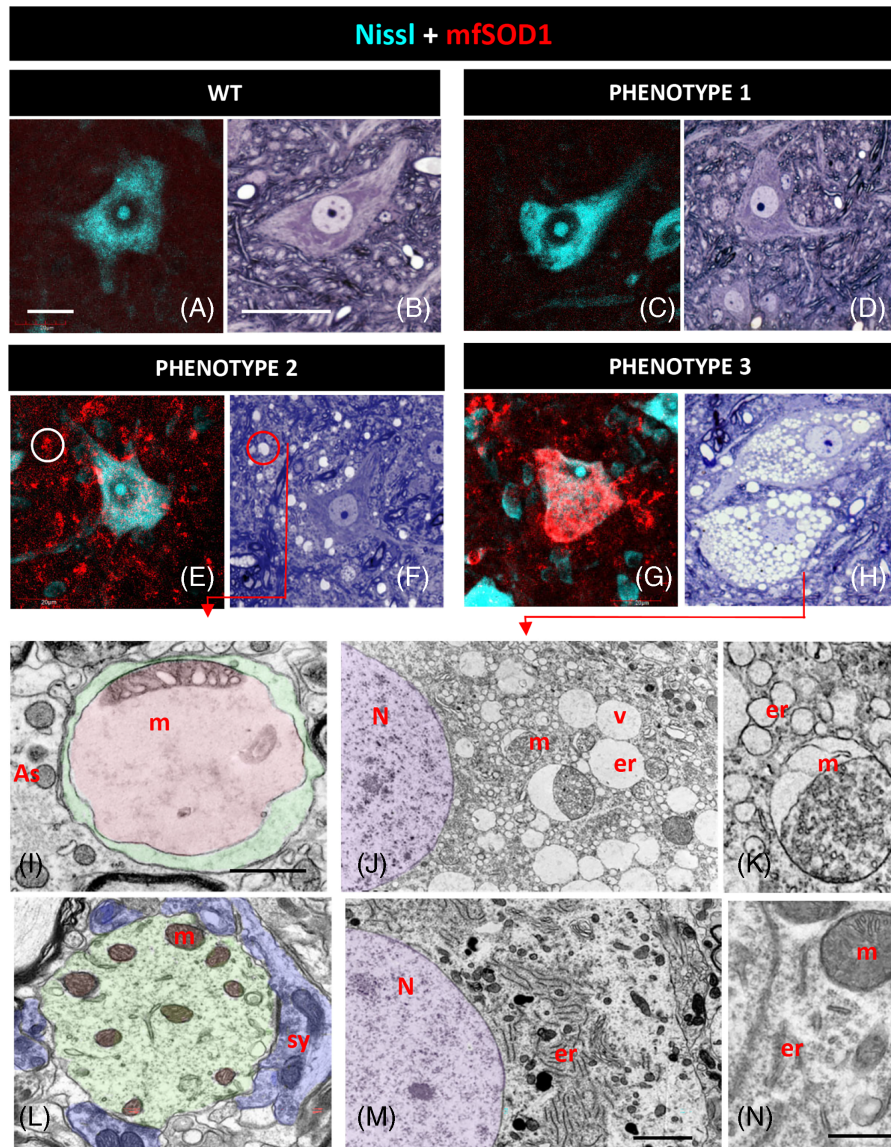
FIGURE 1 MN phenotypes in SOD1^{G93A} mice based on mfSOD1 immunostaining. (A, C, E, G) mfSOD1 signal (red) is depicted combined with Nissl-staining (blue) as indicated. mfSOD1-immunostaining was negative in WT, and absent or very low in phenotype 1 MNs (A, C), but predominates in ventral horn neuropil (circled in E) and MN somata (G) in phenotypes 2 and 3. The mfSOD1 phenotypes are correlated with MN vacuolar changes in semithin sections (B, D, F, H): Vacuoles are absent in WT and type 1 phenotype (B, D), abundant in the neuropil in the type 2 phenotype (F), and extended to the soma in the type 3 phenotype (H). Note the absence of changes in nuclear morphology. (I–N) Ultrastructure of vacuolar degeneration in p60 SOD1^{G93A} MNs (I–K) vs. control WT MNs (L–N), showing images of dendrites (I and L) and somata (J and M). Equivalent regions in semithin sections are indicated by arrows. The mitochondrial origin of vacuoles in dendrites is shown in (I). The cytoplasm of the dendrite (green) is largely occupied by swollen mitochondria (M, red) with a huge expansion of the outer mitochondrial membrane. Comparison to the ultrastructure of a dendrite seen in a control animal (L, green) containing several normal mitochondria (m) and receiving several axodendritic synaptic contacts filled by synaptic vesicles (sy, blue). Synaptic contacts are not observed in the vacuolated dendrite, which is covered by glial processes identified by the absence of clustered synaptic vesicles and the presence of bundles of intermediate filaments (As). The ultrastructure of vacuolated MN somata is shown in (J) and detailed in (K). Equivalent areas taken from control MNs are depicted in (M, N). MNs undergoing vacuolar degeneration (v), displaying fragmentation of the endoplasmic reticulum (er) and enlargement of mitochondrial intermembrane space (m). Remarkably, chromatin ultrastructure (N, violet) remains intact in vacuolated MNs (I, M). All images were taken from P60–P90 asymptomatic or early symptomatic animals. Scale bars: (A) = 20 μm (valid for C, E, G); (B) = 20 μm (valid for D, F, H); (I) = 1 μm (valid for L); (M) = 2.5 μm (valid for J); (N) = 1 μm (valid for K).

that were previously reported [56–60]. In addition, some MNs occasionally exhibited massive fragmentation of their ER into individual vesicles, likely reflecting sustained ER stress and intracellular calcium homeostasis disturbance prior to overt neuronal degeneration and death (Figure S1E,F). Although the MN type 3 phenotype corresponded to severe cellular damage, chromatin condensation was never seen in these neurons (see Figure 1G,H,J,M, and Nissl channel in Figures 5 and 6). In addition, as expected, MN cell bodies with the type 3 phenotype did not display a positive signal for activated caspase 3, confirming the lack of apoptotic machinery
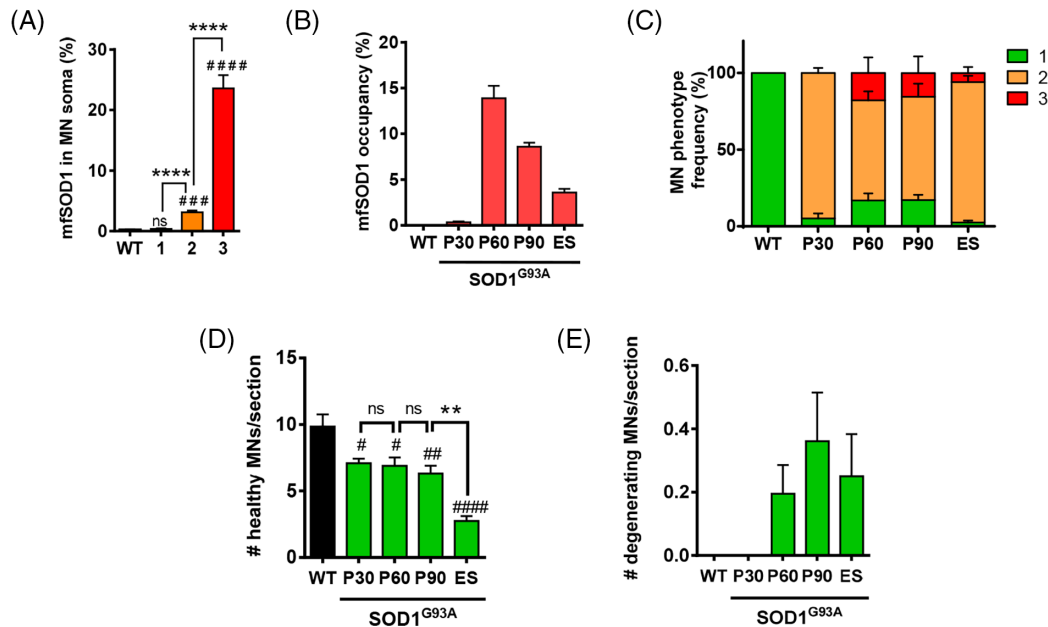
FIGURE 2 mfSOD1 expression, MN phenotypes, and MN death in SOD1^{G93A} mice. (A, B) quantification of mfSOD1 in the MN somata (A) in WT and in the three defined mfSOD1 phenotypes in SOD1^{G93A} mice; (B) the same quantification was performed within ventral horn neuropil in relation to the age-related disease progression (C) quantification of the abundance of the three mfSOD1 MN phenotypes in the ventral horn from WT and in SOD1^{G93A} at distinct stages of ALS progression (ES = end-stage). (D, E) evaluation of the numbers of healthy (D) and degenerating (E) MNs in Nissl-stained spinal cord sections of WT and ALS at distinct ages of progression in SOD1^{G93A} mice. Data in the graph are shown as the mean ± SEM from either 307 MNs or from 17 sections of ventral horn neuropil ($n = 3$ animals per group) in (A and B). (C) Total MNs from 15 to 18 spinal cord sections ($n = 3$ animals per group) were evaluated. ***$p < 0.001$; ****$p < 0.0001$; #$p<0.05$; ##$p<0.005$; ###$p< 0.001$; ####$p<0.0001$ (# refered to WT), one-way analysis of variance (ANOVA), Bonferroni's post hoc test.

activation in these cells (not shown). The ultrastructural morphology of these highly vacuolated MNs fit well in the concept of paraptosis, in which cytoplasmic vacuolation arising from altered mitochondria and/or ER are key features [61,62]. The maximal rise in the emergence of the type 3 phenotype appears between P30 and P90. In this time interval, moderate but sustained MN loss occurred, indicating that MNs with elevated mfSOD1 accumulation died notably during presymptomatic or early symptomatic stages of the disease (Figure 2B–E). Coimmunostaining of mfSOD1 with MMP9 showed that MNs with vacuolar degeneration correspond to the ALS-vulnerable MN subtype (Figure S2A); [63]. The type 3 phenotype was further analyzed by colocalizing mfSOD1 with the mitochondrial and ER markers, showing that mfSOD1 accumulated in large vacuoles of mitochondrial origin and did not share any compartmentation with the ER subcompartments enriched in PDI or BiP (Figure 3K,L) and Figure S2B,C). These EM observations suggested that enlargement of vacuoles of mitochondrial origin occurs because of coalescence of several smaller-sized membrane-bound elements, leading to the generation of large vacuoles with highly expanded intermembrane mitochondrial space. In this way, very large vacuoles (5–10 μm in diameter [-Figure 3F–J, and Figure S1]) can be formed. The multimitochondrial origin of these giant vacuoles can be observed by the presence of segregated elements of internal mitochondrial membrane complexes clustered in a restricted location close to the external vacuolar membrane (Figure 3G). A more precise localization of mfSOD1 was observed on P60 MNs of SOD1^{G93A} mice at the ultrastructural level using the C4F6 antibody and postembedding immunogold labeling (Figure 4A–F). A very clear association of gold particles with medium-sized and large vacuoles present in the soma of MNs displaying the type 3 phenotype was observed. Interestingly, altered but still nonvacuolated mitochondria that were intermixed with vacuoles were devoid of labeling. Mitochondrial-derived vacuoles with largely expanded outer mitochondrial membranes are abundantly present in the soma and in the processes of MNs with type 2 and type 3 phenotypes. In these vacuoles, intense C4F6 immunolabeling was found in the lumen of the vacuole but not in association with remnants of inner mitochondrial membranes that reside, often clustered, at the periphery of the vacuole. In the lumen of the vacuole, gold particles were associated with dispersed material, presumably corresponding to amorphous protein aggregates (Figure 4G). The mfSOD1 accumulation in medium-sized vacuolar structures (∼250 nm) was apparently unrelated to mitochondria, and the absence of labeling in the mitochondria not associated with vacuoles validates our proposal on the biogenesis of large mitochondrial-derived vacuoles from cycles of fusion of mfSOD1-enriched membrane vesicles with the outer mitochondrial membrane and its consequent expansion (Figure 4H).
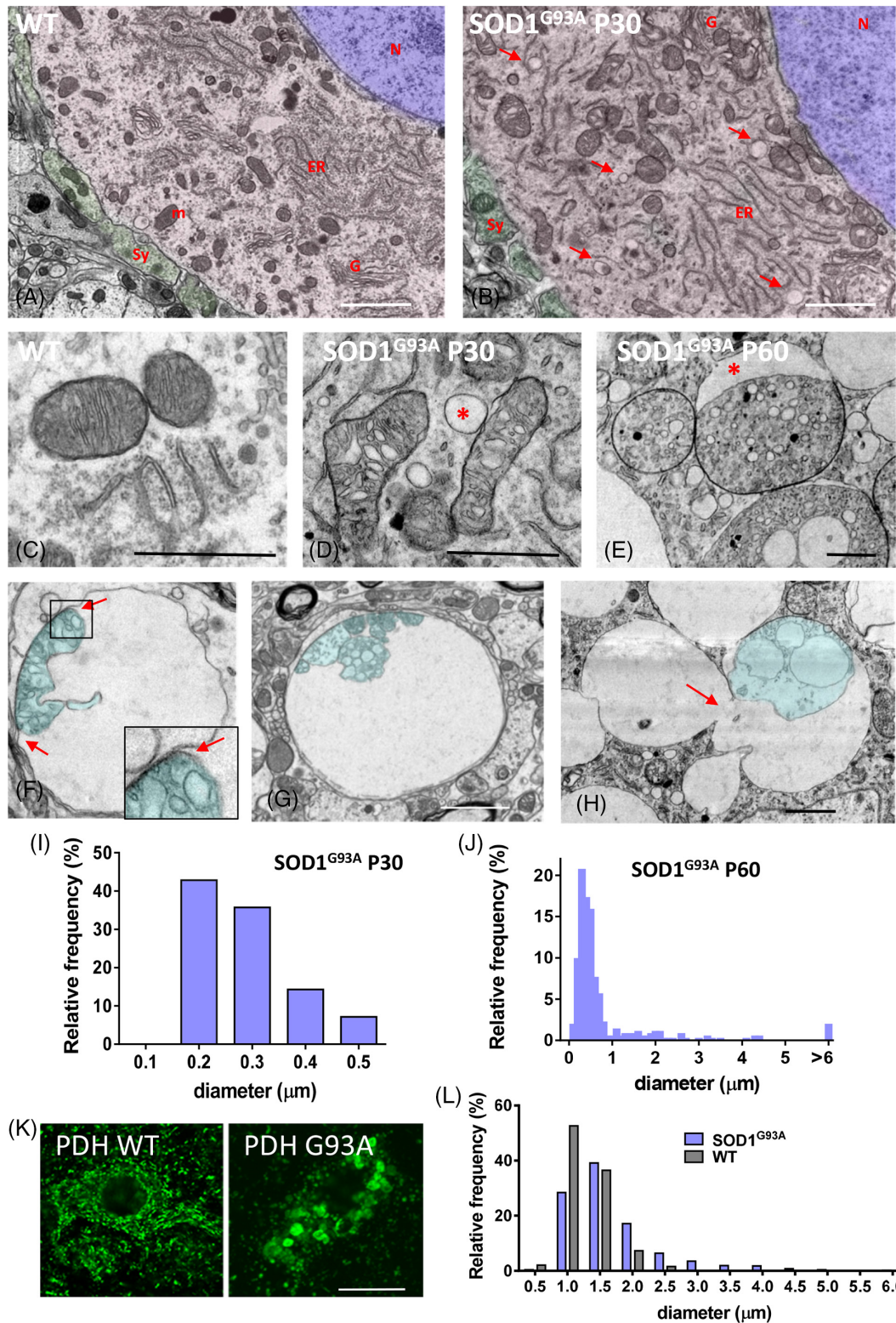
FIGURE 3 Vacuolar degeneration in SOD1^{G93A} MNs. (A, B) low magnification of an EM view of WT and p30 SOD1^{G93A} MN somata showing early vacuolar changes (arrows); MN soma cytoplasms, nuclei, and afferent synapses are dashed in red, blue, and green, respectively (N, nuclei; ER, endoplasmic reticulum; G, Golgi; m, mitochondria; Sy, afferent synapses). (C–E) details of the mitochondrial ultrastructure within MN somata from WT (P30) and SOD1^{G93A} (P30 and P60 as indicated) mice are shown. Note the early swelling of the mitochondrial matrix within the inner mitochondrial membranes in conjunction with early cytoplasmic vacuolization (*) at P30 (D) and its progression, reaching massive vacuolization, with enlargement of the intermembrane space observed at P60 (E). (F) An example of coalescence and fusion of vacuoles seen at P60 is shown (arrow). Swollen remnants of the inner mitochondrial membrane can also be seen (dashed in blue). (G) A giant dendritic vacuole, presumably generated by the fusion of several smaller-sized mitochondria-derived vacuoles originating a single large vacuole, is shown displaying several units of inner membrane complexes clustered at the periphery of the vacuole (blue dashed line). (I,J) frequency distribution histograms of vacuole size measured in P30 and P60 transgenic mouse MN somata; data were taken from two animals of each age. (J) Pattern of immunocytochemical labeling of the mitochondrial marker PDH in WT and P60 SOD1^{G93A} mice. (K) MNs displaying prominent vacuolar changes in mutant mice were quantified and shown in a frequency distribution histogram of the diameter of PDH-positive mitochondrial profiles (mean ± SEM: WT = 1.36 ± 1.28, n = 193 particles in 7 MNs; SOD1^{G93A} = 1.67 ± 0.73, n = 514 particles in 19 MNs); $p < 0.0001$ Student's t-test. Scale bars: (A, B, F, G) = 2 μm; (C–E) = 1 μm; (J) = 20 μm.
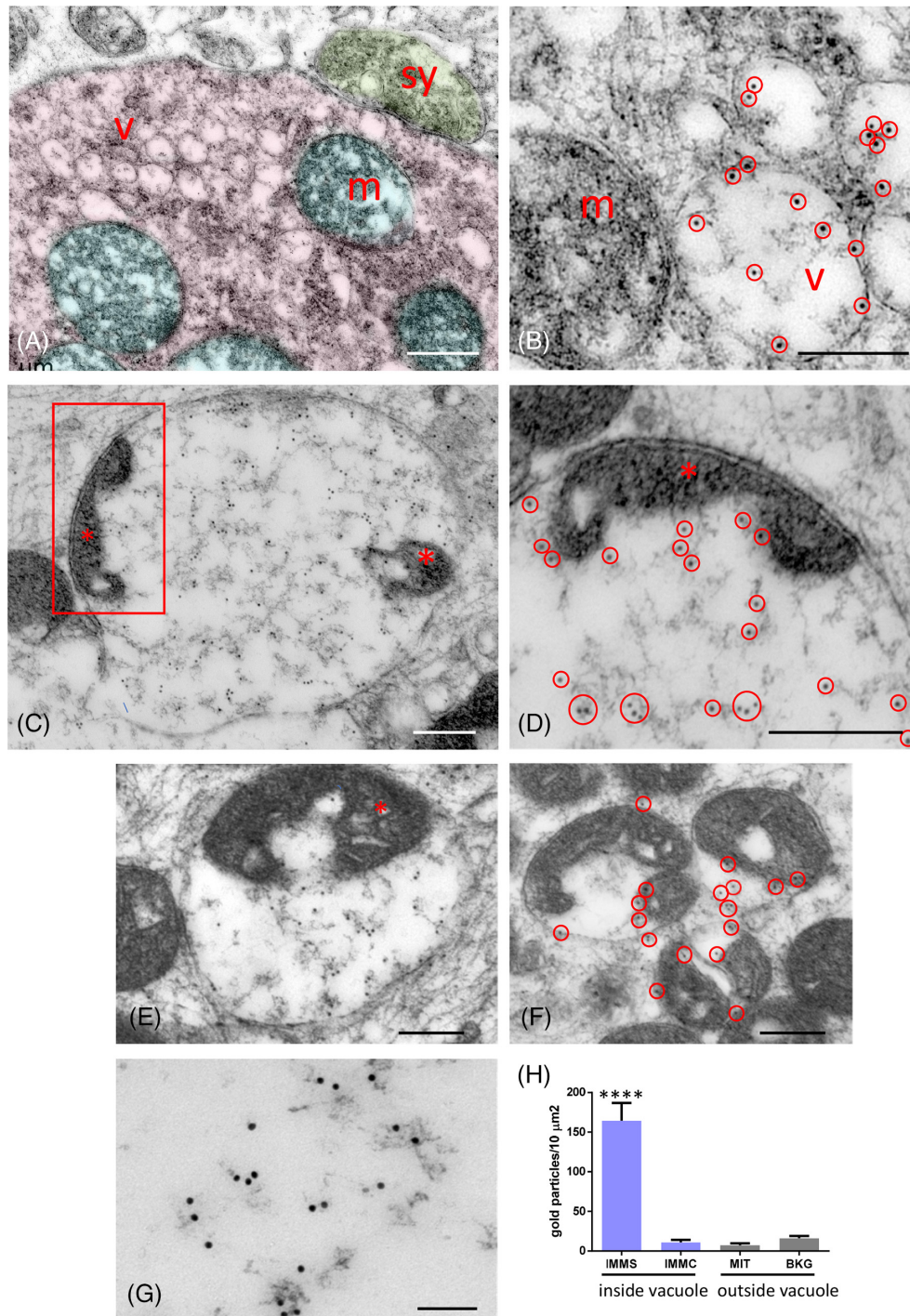
FIGURE 4 Immunoelectron microscopic localization of mfSOD1 on MNs undergoing vacuolar degeneration from P60 SOD1^{G93A} mice. Immunolabeling was visualized using a secondary antibody coupled to 12 nm gold particles. (A, B) an MN soma (shaded in red) filled with medium-sized vacuoles (V) displaying intense immunogold labeling (detailed in b with encircled gold particles). Some altered mitochondria intermixed with the vacuoles (m, shaded in blue) and were devoid of labeling. A synaptic Bouton terminal (Sy) afferent to an MN soma was observed free of labeling. (C) Large mitochondrial-derived vacuole showing an extension of the outer mitochondrial membrane with the corresponding expansion of the intermembrane space. The lumen of the vacuole displays intense mfSOD1 immunolabeling, but the remnants of inner mitochondrial membrane complexes (*) are not labeled. (D) Enlargement of the area delimited in (C) with encircled gold particles. (E) Mitochondria-derived vacuole accumulated in an MN axon displaying characteristic identical labeling as described in (C). (F) Initial steps of biogenesis of mitochondrial-derived vacuoles showing the early expansion of the outer mitochondrial membrane that displays positive C4F6 labeling (encircled gold particles). (G) High magnification detail of C4F6 immunolabeling in the lumen of an MN vacuole. Gold particles are associated with an amorphous, presumably proteinaceous, material. (H) Quantification of immunogold labeling density observed at the distinct subcellular compartments. Within the vacuolar compartment, the intermembrane mitochondrial space (IMMS) and internal mitochondrial complexes (IMMC) were analyzed separately. MIT is the number of mitochondria within vacuolated MNs but outside the vacuoles, and BKG represents the background signal. ****$p < 0.0001$, one-way analysis of variance (ANOVA), Bonferroni's post hoc test (IMMS bar vs any other). Scale bar: (A) = 500 nm; (B) = 250 nm (valid for C–F); (G) = 100 nm.
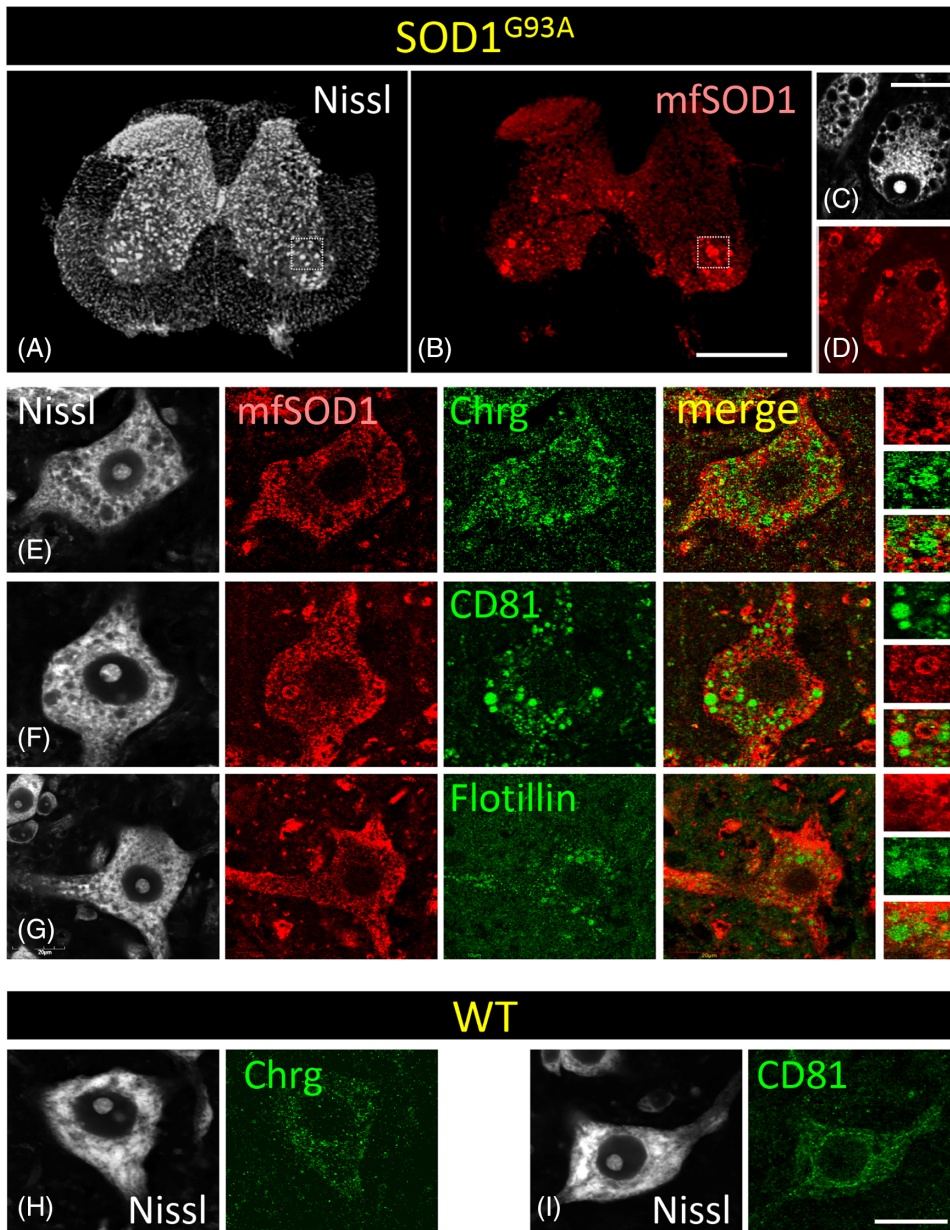
FIGURE 5 Immunocytochemical characterization of MN vacuolar degeneration. (A, B) in low magnification images of the whole spinal cord, a scarce number of neurons displaying strong mfSOD1 are seen located at the ventral horn (B). In the enlarged insets (delimited in B), a detail of a mfSOD1-positive MN showing its associated vacuolar degeneration is evidenced after Nissl costaining (C, D). (E–I) MNs displaying high immunoreactivity to mfSOD1 using a C4F6 antibody (red) were coimmunostained with several antibodies as indicated (green). Samples were taken from P60 SOD1^{G93A} or WT mice and counterstained with Nissl (gray). In each row, the details of mSOD1 (red) and the corresponding protein signal are depicted in separate channels, and merged images are shown in the insets. Scale bars: (B) = 500 μm; (C, I) = 20 μm (valid for the rest of the panels, except insets).

We hypothesized that the ultimate fate of vacuoles massively accumulating in degenerating MNs should be their release to the extracellular space in the form of extracellular vesicles (EVs). For this reason, we further explored the distribution of additional markers in vacuolated and mfSOD1-enriched MNs (Figure 5A–G). Strong positive immunoreactivity for chromogranin (Chrg) was observed in the lumen of many, but not all, large cytoplasmic vacuoles in MNs with the type 3 phenotype but not in WT MNs (Figure 5H). Chrg+ granules also displayed positive signals for mfSOD1 and PDH (Figures 5E and 6A). Chrg is a protein found in secretory vesicles in neurons and neuroendocrine cell systems. It has been reported that Chrg interacts with mutant SOD1, which is abnormally secreted at the extracellular space in ALS [64]. Our data on the colocalization of mutant SOD1 with Chrg agree with this previous report, and its coexistence with a mitochondrial protein marker indicates heterogeneity with respect to the vacuole origin and contents. Moreover, highly positive CD81 immunoreactivity was observed in association with large cytoplasmic vacuoles, contrasting with the fine punctate pattern of CD81 observed in WT MNs (Figure 5F,I). CD81 is a member of the tetraspanin family of proteins that is enriched in EVs or exosomes [65], including those of neuronal origin [66]. However, other members of the tetraspanin family, such as CD9 or CD63, were not found in MN vacuoles in a similar way to that described in some EV subtypes [65]. A positive signal for flotillin, another well-established EV marker, was also detected in relation to MN vacuolar degeneration (Figure 5G). In addition, some of these paraptotic-like MNs contained pMLKL-positive

FIGURE 6 mfSOD1-containing vacuoles share positivity for PDH and for nonmitochondrial proteins such as Chrg and CD81. (A) Chrg immunostaining (green) was combined with mfSOD1 labeling by means of the C4F6 antibody (red) in vacuolated P60 MNs from SOD1^{G93A} mice (gray). In the enlarged panels, a detail of the area delimited in (A) is shown below, together with the pixel intensity profile of both channels along the indicated line. (B) CD81 immunostaining (green) was combined with the mitochondrial protein marker PDH (red) in vacuolated P60 MN from SOD1^{G93A} mice (gray). In the enlarged panels, a detail of the area delimited in (B) is shown below, together with the pixel intensity profile of both channels along the indicated line. Scale bar: (A) = 20 μm (valid for the rest of the panels, except insets).
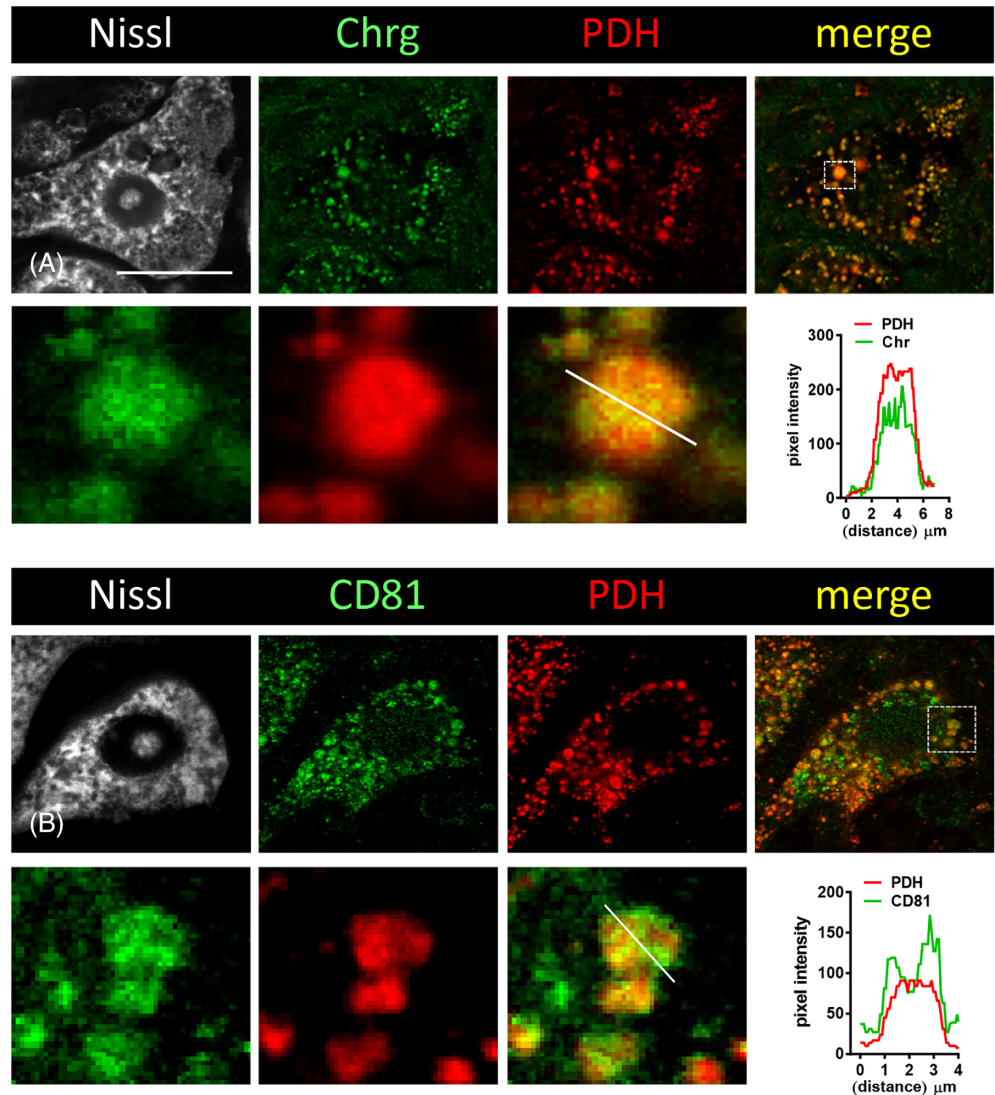
granules, suggesting that a mechanism of membrane rupture, as occurs during the execution of necroptotic cell death [67], may be activated in vacuolated MNs. Conversely, MNs with low levels of mfSOD1 did not contain pMLKL-positive particles (Figure 7A–I). This suggests that the final fate of vacuolated MNs is membrane disruption with a massive release of necroptotic-like vesicles. Western blot analysis of pMLKL protein revealed clear upregulation in spinal cord extracts at the end stage of disease but not before (Figure 7J,K and Figure S3). The scarce representation of protein in the whole spinal cord at P60–90 likely made it only detectable by immunocytochemistry at these earlier stages. Many vacuoles containing either Chrg or CD81 also showed a positive signal for the mitochondrial marker PDH (Figure 6A,B). This aberrant localization of nonmitochondrial proteins into mitochondrial compartments reflects the multiorganelle origin of vacuoles generated by coalescence and fusion of a variety of membrane-bound elements, as suggested after EM examination. Notably, EVs of mitochondrial origin (mitovesicles) have been recently

described in the brain; these vesicles share EV markers with mitochondrial proteins [68]. In agreement with Rudnick et al. [69], we also observed p62-positive round bodies that were highly homogeneous in size (2.94 ± 0.06 μm of diameter, $n = 72 ±$ SEM) in some vacuolated, mfSOD1-positive MNs, indicating that the dysregulation of autophagy also exists in these early degenerating MNs (Figure 8A,B). Although these MNs corresponded to the type 3 phenotype, the p62-positive round inclusions did not correspond to aggregates of mfSOD1 (Figure 8A); rather, they were enriched in ubiquitinated proteins (Figure 8C). In contrast to the round bodies, p62-positive skein-like inclusions were also observed in scarce p60 ventral horn neurons that were negative for mfSOD1 (Figure 8A). These results are in concordance with those previously reported [69]. We additionally observed that p62-positive round inclusions in vacuolated MNs are, in fact, mitochondria that display a p62-positive coat (Figure 8D). This is consistent with the role of p62 in the ubiquitination of mitochondrial proteins during mitophagy [70].
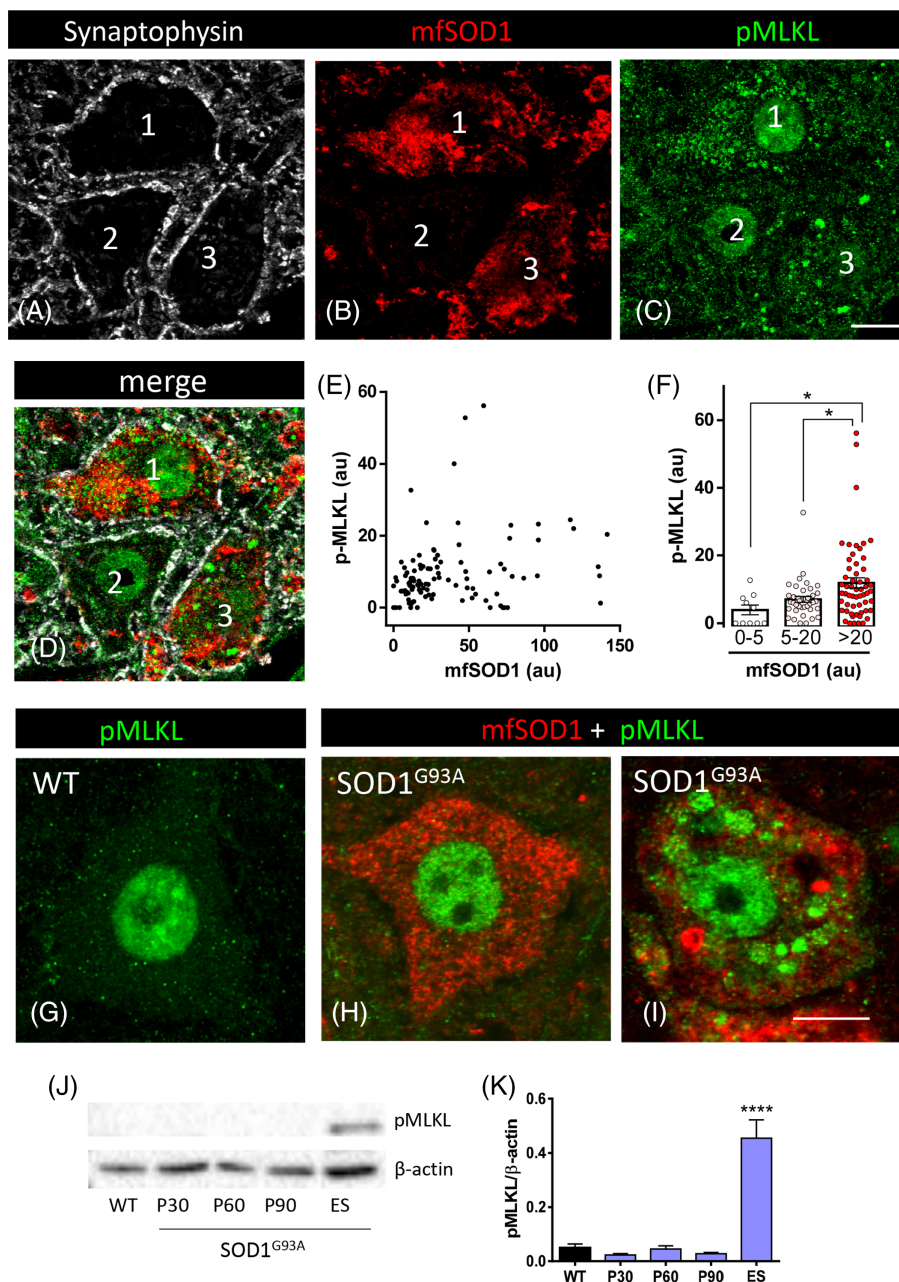
FIGURE 7 Association of necroptotic vesicles with MNs displaying mfSOD1 accumulation and vacuolar degeneration. (A) Three MN cell bodies were delimited by their afferent synaptic boutons (synaptophysin immunostaining, gray) and numbered in a ventral horn of P60 transgenic mice. (B) Immunolabeling for mfSOD1 (red) shows a variable signal among these MNs ranging from high (1 and 3) and low (2) intensity. (C) Coimmunostaining for pMLKL demonstrates the accumulation of necroptotic vesicles in MNs 1 and 3, which are enriched in mfSOD1 but not in MNs 2, in which the mfSOD1 signal is faint. (D) A merged three-channel image is depicted. (E) the intensity of mfSOD1 and pMLKL immunoreactivity was measured in the soma of 106 MNs ($n = 4$; P60–P90 SOD1^{G93A} animals) and individually plotted in the graph. (F) The whole analyzed MN population was further divided into three groups for assessing their pMLKL in relation to the mfSOD1 content; the groups represent low (0–5), middle (5–20), and high (>20) mfSOD1 according to the intensity of their immunoreactive signal in arbitrary units (au). (G–I) an example of pMLKL immunoreaction (green) on a MN soma from WT (G) or P60 SOD1^{G93A} MNs with high mfSOD1 content (red) representing type 3 phenotype (H and I); note that pMLKL vesicles are absent in (H) but present (I), suggesting that necroptosis is the ultimate fate of MNs once mfSOD1 accumulation occurs. pMLKL-immunoreactivity within the nucleus was not evaluated as a marker of necroptosis as it was also seen in WT (G). *$p < 0.05$, one-way ANOVA, Bonferroni's post hoc test. (J, K) Western blot analysis of pMLKL in spinal cord extracts of WT and transgenic mice at different age points as indicated (ES = end-stage). Densitometric quantification is also shown in (K) after measurements performed in three independent experiments on three animals at each point. ****$p < 0.0001$, one-way ANOVA, Bonferroni's post hoc test (ES bar vs any other). Scale bars = 10 μm.

Overall, our data on the immunocytochemistry of MN vacuolar inclusions allow the discrimination of three subtypes of inclusions in vacuolated MNs: (i) those

sharing positivity for mfSOD1, PDH, Chrg, CD81, and flotillin, which are the most abundant and highly variable in size; (ii) those that were p62- and ubiquitin-positive but

FIGURE 8 Mitophagic nature of a subset of mitochondrial-derived inclusions observed in MNs undergoing vacuolar degeneration. (A) p62 immunostaining (green) was visualized in conjunction with mfSOD1 (red) and fluorescent Nissl staining (gray) in two delimited MNs (1 and 2) from P60 SOD1^{G93A} mice, revealing two types of inclusions: (1) skein-like in an MN negative for mfSOD1 and (2) round bodies in an MN positive for mfSOD1. (B) An enlarged image of p62-positive round inclusions in MN 1 is depicted in conjunction with the mfSOD1, together with a pixel intensity profile along the indicated line. Note the absence of mfSOD1 enrichment in the p62-positive round inclusion;. (C) p62-positive inclusion (green) in conjunction with ubiquitin immunostaining (red) and a pixel intensity profile along the represented line are shown. (D) Round p62-positive inclusions (green) display positivity for the mitochondrial marker PDH (red) in a P60 SOD1^{G93A} MN undergoing vacuolar degeneration, as shown after Nissl staining (gray). An enlargement of the delimited area is depicted below, including a pixel intensity profile along the indicated line in a selected mitochondrion outlined by p62, which is indicative of mitophagy. (E) CD81, p62, and pMLKL (green) profiles seen in SOD1^{G93A} MNs undergoing vacuolar degeneration (Nissl, gray) were analyzed for density and size, as shown in the adjacent graphs: Ns = non significant; *$p < 0.05$, ****$p < 0.0001$, one-way ANOVA, Bonferroni's post hoc test. Scale bar: (A, D, and E) = 20 μm.
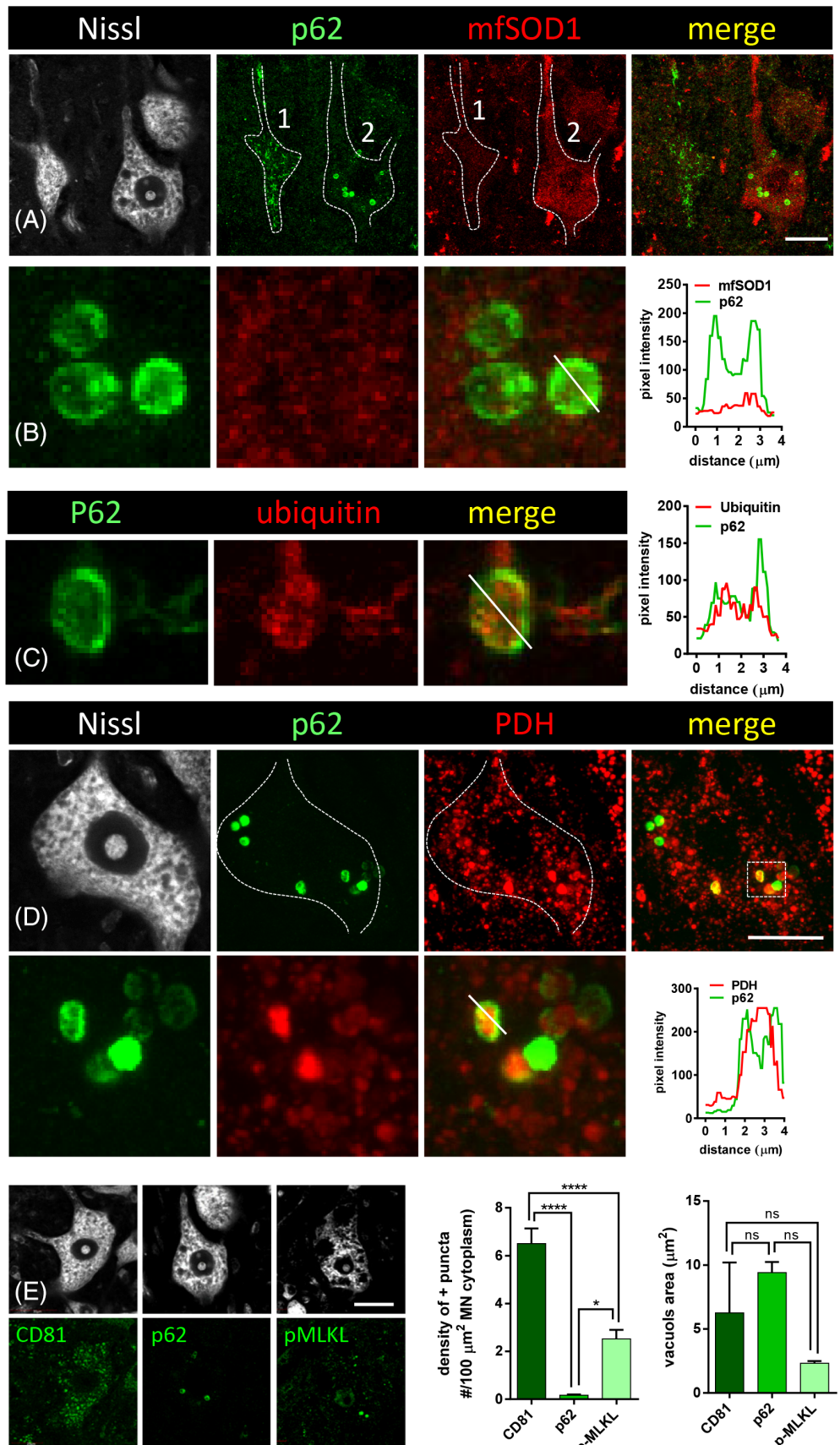
mfSOD1-negative, exhibiting remarkable size and shape equality; and (iii) those displaying pMLKL positivity, presumably representing necroptotic vesicles (Figure 8E).

Thus, the significant (~60%) reduction of the type 3 phenotype at the end stage is a consequence of the massive MN cell death that takes place once symptomatology has started after P90 (Figure 2D). This indicates that ALS-resistant MNs, which still remain at the end stages of the disease, do not accumulate particularly large amounts of mfSOD1. Importantly, the scarcity of the type 3 phenotype at end stages did not indicate a reduction in neuronal death. Conversely, as MN death is maximal in this period, the phenotype of dying neurons did not imply mfSOD1 accumulation associated with vacuolar morphology. Instead, most degenerating MNs seen in the ventral horn at end-stages displayed disorganization of the normal intracellular organelle architecture, with a marked ER disassembly, altered Golgi network, and prominent accumulation of presumably small transport vesicles (Figure S4A,B); these vesicles are clearly distinct in size and shape from those described in phenotype 3 MNs. In addition, in degenerating MNs of terminal animals, almost none of the mitochondria displayed massive vacuolar degeneration, greatly contrasting with the MN type 3 phenotype. Other MNs at the end stage displayed complete organelle disruption and amorphous intracellular inclusions, which corresponded to large protein aggregates (Figure S4C). Overall, these results indicate the coexistence of a diversity of mechanisms of neuronal death during ALS progression.

3.2 | Synaptic inputs to MNs and mfSOD1 accumulation

Alterations in synaptic inputs and MN excitability have been reported as early events in ALS [15,57,58,71–78]. By examining the density of synaptic terminals on MN cell bodies using synaptophysin immunolabeling, we did not observe any significant change between SOD1^{G93A} and WT animals at P60 (synaptic puncta/100 μm MN perimeter: WT $= 102.1 \pm 1.55$, SOD1^{G93A} $= 106.1 \pm 1.39$ [mean $\pm$ SEM]; $n = 299$ and 383 MNs, respectively, from three animals per condition; $p > 0.05$). However, a significant loss of afferent axosomatic synapses was detected in SOD1^{G93A} mice when the analysis was restricted to MNs displaying the type 3 phenotype with extensive vacuolization and mfSOD1 accumulation (Figure S5): synaptic puncta/100 μm MN soma perimeter: SOD1^{G93A} MNs with type 3 phenotype $= 91.01 \pm 2.3$ vs. the entire population of SOD1^{G93A} MNs $= 106.1 \pm 1.39$ [mean $\pm$ SEM], $p < 0.0001$; $n = 147$ MNs from three animals. However, it appeared that the activity of afferent inputs on SOD1^{G93A} MNs underwent more widespread changes, which were reflected by alterations in the ultrastructural organization of presynaptic organelles (Figure S6A–D). Indeed, the density of small (<100 nm) vesicles contained within afferent synaptic boutons on MNs was markedly reduced at P60 but not at P30 in SOD1^{G93A} mice (Figure S6E). This vesicle depletion occurred irrespective of the S (excitatory) or F (inhibitory) synaptic type [79]. In addition, many synaptic terminals at P60 contained an abnormal accumulation of large endosome-like vacuoles (> 100 nm in diameter), which presumably indicates altered synaptic vesicle recycling because of dysregulated neurotransmitter release (Figure S6C,F). Pioneering studies on the relationship between synaptic structure and function have shown that increased synaptic activity results in the accumulation of complex vesicles and presynaptic endocytic structures generated as a consequence of the blockade of the vesicle recycling process [80–83].

The ultrastructure of presynaptic boutons in advanced stages of the disease displayed extreme degenerative changes and presynaptic membrane disruption with the release of vesicular structures into the extracellular space (Figure S6D). Similar changes have been reported to occur in acute degeneration of synaptic terminals in axotomized MNs and involve activation of the necroptotic pathway [24].

Regulation of MN excitability particularly depends on the activity of cholinergic C-type synapses (C-boutons) through a decrease in the after-hyperpolarization potential [84]. Although controversial [85], changes in C-bouton size or density have been reported in ALS [15,86–91]. Using double immunolabeling for VAChT and NRG1, the pre- and postsynaptic compartments of C-type synapses can be delimited [92,93], and their changes in relation to the already defined misfolded SOD1^{G93A} MN phenotypes can be examined. After coimmunostaining with anti-mfSOD1 antibodies, we found that quantitative alterations in VAChT were observed in MNs exhibiting the type 2 and 3 phenotypes, whereas postsynaptic organization, visualized by NRG1 labeling, shows a tendency to be altered in the less severe phenotype and, more clearly, in early stages of disease (Figure 9A,B); this change, however, did not reach statistical significance. NRG1 is a protein coclustered with other molecules forming part of the signaling complex associated with the subsynaptic cistern of C-boutons [92,94,95].

It should be noted that in MNs at early stages of disease (P30) or in those exhibiting middle severity alteration (type 2 phenotype), presynaptic VAChT-positive C-bouton terminals are moderately, but significantly, enlarged in SOD1^{G93A} animals. This is consistent with previously reported findings [15,87,89,91]. Thus, alterations in C-bouton signaling may be relevant for determining MN dysfunction prior to cell death. For this reason, we analyzed the impact of a pharmacological intervention on C-bouton signaling on mfSOD1 accumulation in MNs. We applied treatments with the M2 muscarinic cholinergic receptor agonist oxotremorine or antagonist methoctramine, according to established protocols [15]. The effects of these drugs on the expression of mfSOD1 and C-bouton morphological parameters were examined after 15 days of treatment started on p60 (Figure 9C). Methoctramine significantly promoted the expression of mfSOD1 in the ventral horn. Both treatments
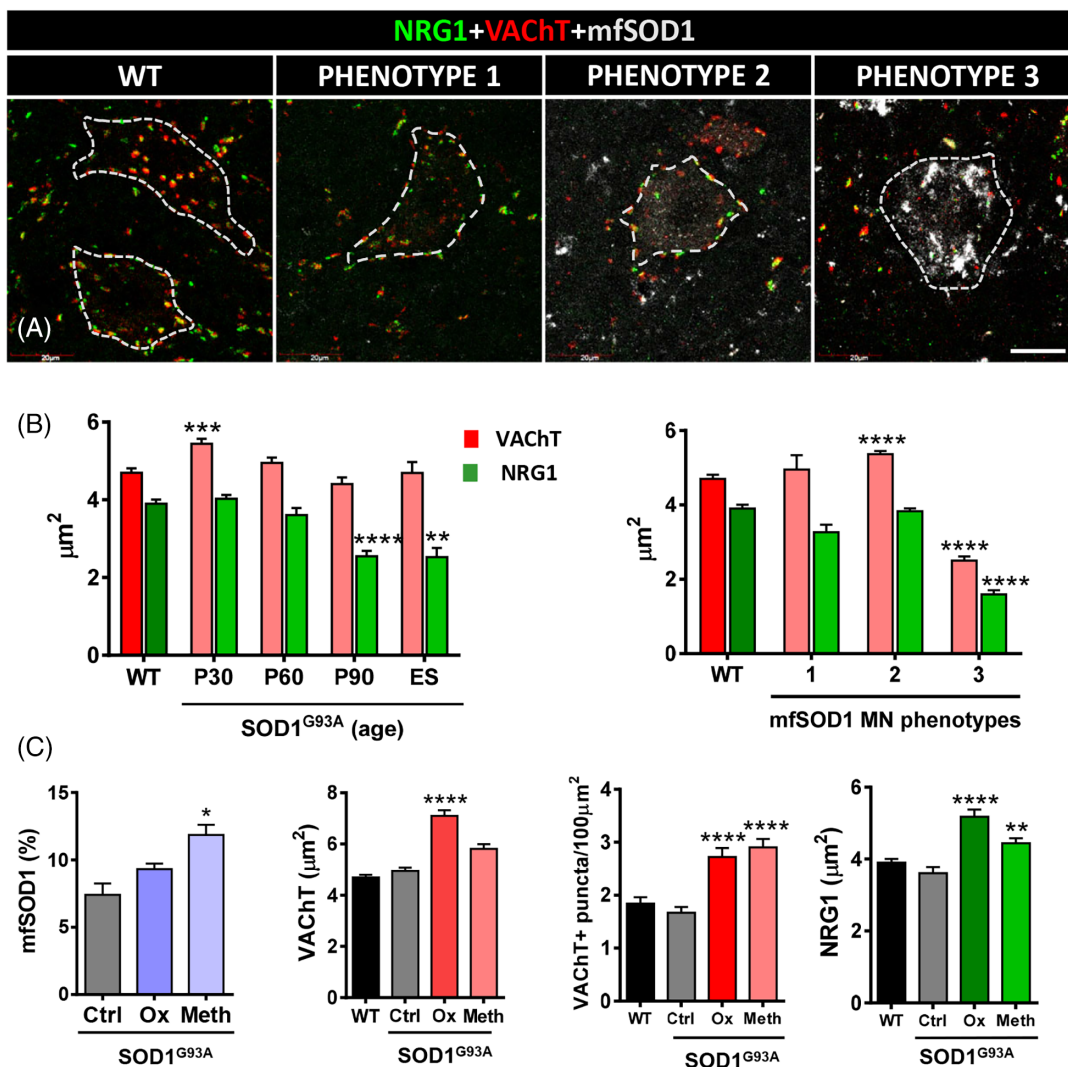
FIGURE 9 C-type synaptic boutons and mfSOD1 MN phenotypes in SOD1^{G93A} mice. (A) C-type synapses in MN somata (delimited by a line drawn on a not shown Nissl image) were analyzed after labeling their postsynaptic and presynaptic compartments to visualize NRG1 (green) and VAChT (red), respectively, in WT and P60 SOD1^{G93A}, as indicated. C-Bouton imaging was merged with mfSOD1 immunostaining (gray) to identify the three MN phenotypes. (B) Changes in the size of pre- and postsynaptic components of C-boutons evaluated at distinct disease ages in relation to MN mfSOD1 phenotypes vs control. (C) Effects of treatments with the M2 muscarinic cholinergic receptor agonist (oxotremorine, ox) or antagonist (methoctramine, meth) of P60 SOD1^{G93A} mice on the expression of mfSOD1 and C-Bouton size 15 days after treatment. Sample sizes were as follows: WT, $n = 193$; SOD1^{G93A}, $n = 219$; ox, $n = 167$; meth, $n = 202$; $n =$ synapse number s from 3 animals. One-way ANOVA: $p < 0.0001$, ox vs. control; $p < 0.01$, meth vs. control data for presynaptic C-Bouton density were as follows: WT, $n = 37$; SOD1^{G93A}, $n = 59$; ox, $n = 46$; meth, $n = 24$ VAChT-positive puncta/100 μm^2; $n =$ number of MNs from 3 animals. *$p < 0.05$, **$p < 0.01$, ***$p < 0.001$, ****$p < 0.0001$, one-way ANOVA, Bonferroni's post hoc test. Scale bar: (A) $= 20\ \mu m$.

resulted in a similar effect, increasing the number and size of VAChT-positive C-bouton terminals. Similar changes were found in the size of NRG1 spots, representing the postsynaptic side of C-boutons; however, no changes were observed in the density of NRG1 spots on MN somata after these treatments.

3.3 | Glial responses and mfSOD1 accumulation

A critical aspect of ALS pathology is glial activation, which affects the onset and progression of disease [10,96–101]. Microglial activation results in cell proliferation and phenotype switching from a protective anti-inflammatory state to a neurotoxic state exhibiting pro-inflammatory features [102,103]. Microgliosis is particularly prominent at advanced stages of disease but has also been detected presymptomatically either by histological analysis or by molecular signature [104,105].

The extent of astrogliosis and microgliosis in relation to mfSOD1 expression in the spinal cord ventral horn was analyzed in SOD1^{G93A} mice during disease progression. This was accomplished after triple fluorescent immunolabeling for GFAP, Iba1, and C4F6. All markers showed a progressive and parallel rise, indicative of both
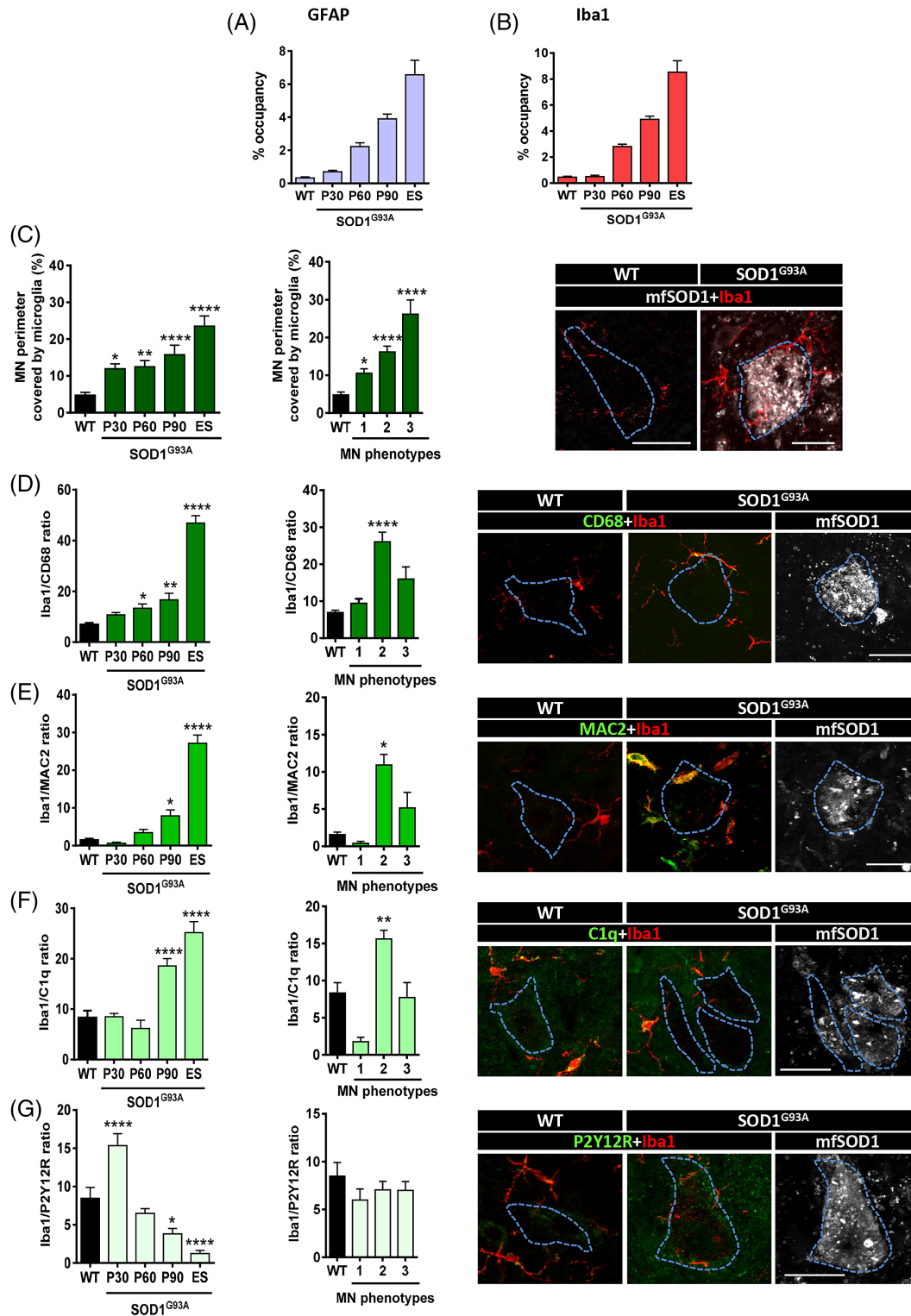
FIGURE 10 Phenotypic characterization of microgliosis during disease progression and its relation to the mfSOD1 MN phenotypes. (A, B) As an index of global glial reaction, quantification of ventral horn neuropil occupancy by astrocytes (GFAP, A), and microglia (Iba1, B) in WT (P120) and SOD1^{G93A} mice was performed at different ages of disease progression in the whole ventral horn. (C–G) Additional measurements were performed on recruited microglia interacting with MN somata as indicated. On each row, representative images of the corresponding markers (green) in combination with Iba1 (red) and mfSOD1 (gray) are included for the WT and the type 3 phenotype. Data are shown as the mean ± SEM, from 15 to 20 MN neuropil sections (A, B) and from 20 to 50 MN neuropils (C–G), from three mice under each condition; *$p < 0.05$; **$p < 0.01$; ****$p < 0.0001$, one-way ANOVA, Bonferroni's post hoc test. Scale bars: (A) = 30 μm (valid for D–H).

astrogliosis and microgliosis, from P30 to the end stages of disease. However, expression of mfSOD1 did not follow a similar parallel course, with a rapid rise between P30 and P60, followed by a subsequent gradual decline. Interestingly, at the end-stage period, the content of mfSOD1 was notably reduced, likely because of a substantial loss of MNs involving those of the type 3 phenotype (Figure 2B).

A more detailed analysis of the microglial reaction occurring in close apposition with MN cell bodies was also performed in relation to their mfSOD1 content and phenotypes. These results are shown in Figure 10C–G. MN cell bodies closely interacted with recruited microglial cells and were positively correlated with disease progression. Moreover, cell bodies expressing high levels of mfSOD1 were largely covered by microglia. A parallel increase in the number of CD68+ lysosomal particles within Iba1-delimited microglia profiles, indicative of their phagocytic activity, was observed. A similar profile was found for the expression of galectin-3/Mac-2, a marker for a subset of activated-phagocytosing microglial cells [106], and for the inflammatory molecule C1q. However, when Iba1-positive microglia were co-immunostained for P2Y12R, an inverse time course profile was observed, with maximal expression at presymptomatic stages (P30) following a subsequent decline reaching minimal levels at end-stages. P2Y12R is a subtype of G-coupled purinergic receptor uniquely expressed in CNS microglia [107] that is strongly downregulated in its activated states when microglia progress from ramified to amoeboid morphology [108]; this assumption is fully consistent with our data in ALS mice.

In addition to longitudinal analysis during the evolution of ALS, when microglia were topologically analyzed in relation to MN mfSOD1 phenotypes, it was found that all markers of activation were elevated around MNs in type 2 and 3 phenotypes, whereas levels of P2Y12R were not affected by the proximity of mfSOD1 deposits.

3.4 | Elimination of microglia reduces the severity of MN phenotypes of mfSOD1

PLX5622 is a CSF1R inhibitor that, when administered orally in mice, results in the virtual elimination of the entire microglial population [34]. By applying this drug, we examined how the absence of microglial cells affected the expression of mfSOD1 in SOD1^{G93A} animals. Iba1 immunostaining was performed at P30 in animals that had been treated with PLX5622 for 30 days, which resulted in a lack of detectable microglia in spinal cord sections. This treatment also provoked a reduction in mfSOD1 expression when analyzed at P60. The percentage (mean ± SEM) of mfSOD1 immunoreactivity occupancy found in the ventral horn was WT = 0.18 ± 0.02 [$n = 32$]; SOD1^{G93A} P60 = 7.4 ± 0.86 [$n = 29$]; SOD1^{G93A} P60-PLX5622 = 3.45 ± 0.39 [$n = 52$] (SOD1^{G93A} P60

vs. SOD1^{G93A} P60-PLX5622, $p < 0.05$ [one-way ANOVA]; n = number of measurements from 3 animals per condition). Of note, mfSOD1-immunoreactive vacuolated (type 3 phenotype) MNs were markedly depleted in the absence of microglia, as shown by the analysis of C4F6 signal occupancy on P60 MN somata (WT = 0.23 ± 0.04 [$n = 62$]; SOD1^{G93A} P60 = 12.69 ± 1.75 [$n = 54$]; SOD1^{G93A} P60-PLX5622 = 2.4 ± 0.21 [$n = 95$]; $p < 0.0001$, SOD1^{G93A} P60 vs. SOD1^{G93A} P60-PLX5622 [one-way ANOVA]; n = number of measurements from 3 animals per condition).

3.5 | Effects of peripheral nerve injury in SOD1^{G93A} mice on the progression of MN pathology

According to the "dying-back" hypothesis, it has been proposed that ALS is initiated as a distal axonopathy that evolves to proximal axonal degeneration, leading to an altered retrograde-signaling cascade resulting in MN death [21,109]. The interruption of neuromuscular connections because of peripheral nerve injury is also a strong negative modifier of the ALS phenotype in animal models [110–112]. Nevertheless, some positive effects promoting regenerative events and MN survival were also observed after nerve crush in SOD1^{G93A} mice [113,114]. Here, we examined whether sciatic nerve transection (axotomy), performed in SOD1^{G93A} mice, alters the expression of mfSOD1 MN phenotypes and promotes neuroinflammation in the spinal cord. The MN pool located at the Pes9 region of the lumbar 6 spinal cord segment, which corresponds to the location of the injured MNs [36], was analyzed 7 days following axotomy performed at distinct time points of disease progression (P30, P60, and P90). In all conditions, we observed a shift in the relative amount of the three MN phenotypes to those that are more harmful as a consequence of nerve transection (Figure 11). For example, at a presymptomatic stage (P30) in which MN phenotype type 3 did not appear in unoperated SOD1^{G93A} mice, sciatic nerve axotomy resulted in an induction of this more severe cytopathological phenotype, affecting ~24% of MNs. Nerve axotomy performed at later stages, such as P60 or P90, also entailed a worsening in the MN phenotype score (Figure 11B). It is well known that peripheral nerve lesions induce a plethora of changes in axotomized MN cell bodies and in adjacent synaptic afferents and glial cells [24,115]. We found here that the strong neuroinflammatory response induced prematurely by axotomy in SOD1^{G93A} animals acts as a synergistic mechanism in promoting mfSOD1 expression (Figure 11C,D). This also indicates a link between the expression of neurotoxic forms of SOD1 in MNs and neuroinflammation. It is conceivable that injury-mediated microgliosis, when produced under a SOD1^{G93A} background, may exacerbate the endogenous neurotoxicity of microglia that basally exists as a consequence of the disease [19,116]. Conversely, mfSOD1
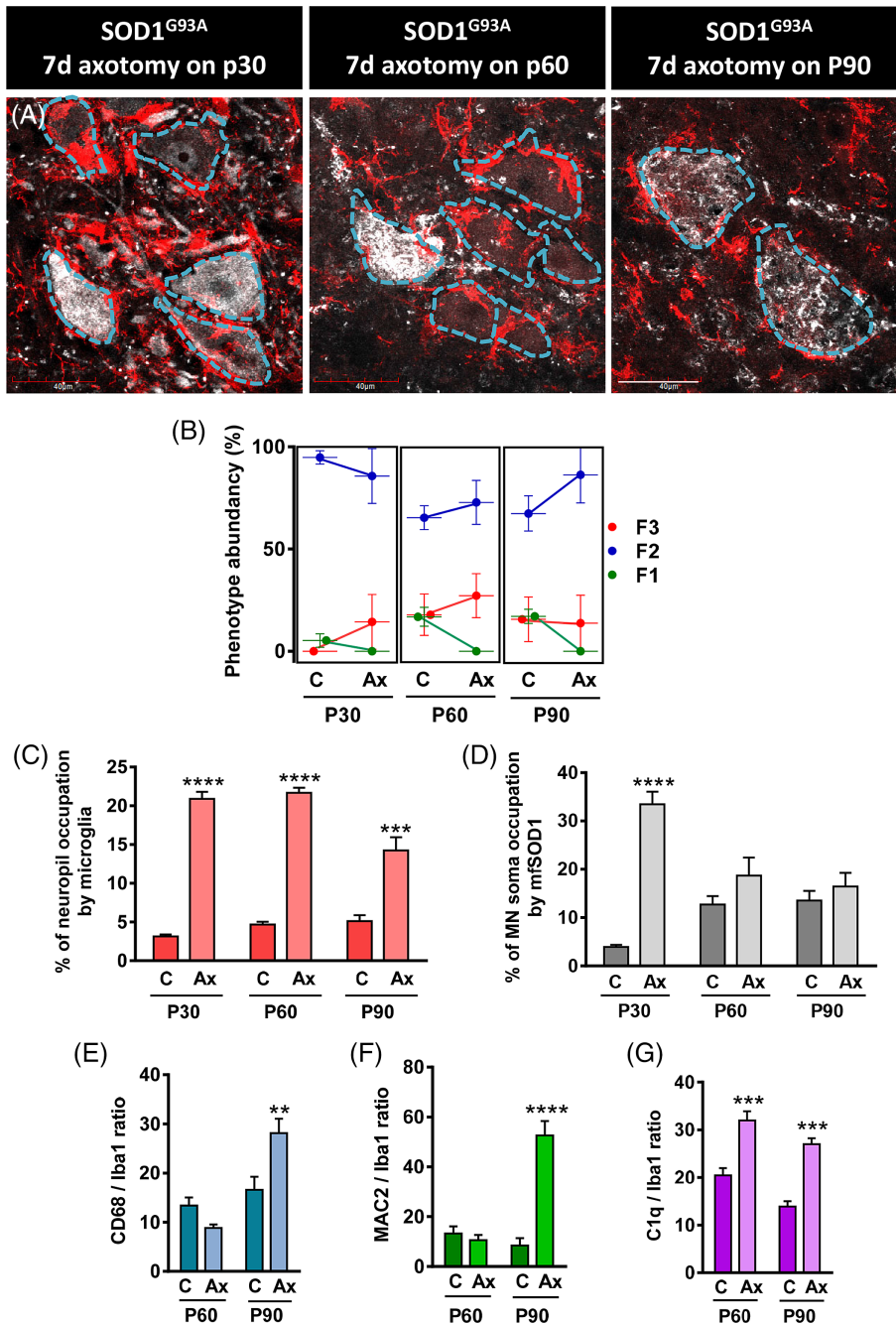
FIGURE 11 mfSOD1 and microglia in SOD1^{G93A} mice after sciatic nerve transection. (A) MN somata (delimited by lines drawn on the not shown fluorescent Nissl channel) were coimmunoprecipitated for microglia (Iba1, red) in conjunction with mfSOD1 (gray) and examined 7 days after axotomy performed at different ages. (B) The mfSOD1 phenotype abundancy was evaluated in control and axotomized ventral horns from transgenic mice, as indicated. (C–F) Quantification of the effects of axotomy on ventral horn microglial reaction (C) and mfSOD1 expression (D) surrounding axotomized MN pool and within axotomized MNs, respectively. The degree of expression of some markers of microglial activation was further assessed (E–G). Each condition was compared to age-matched transgenic mice. Data for graphs are shown as the mean ± SEM from three animals as follows: In (B) from the total MNs present in sections of 3 different animals; in (C) from 17 to 82 MN neuropil in (D–G) from 20–60 MN somata. **p<0.01, ***$p < 0.001$, ****$p < 0.0001$, one-way ANOVA, Bonferroni's post hoc test. Scale bar: (A) = 40 μm.

accumulated in degenerating MNs and could be released in the extracellular medium via exosomal or necroptotic-like EVs; as extracellular mfSOD1 is a potent trigger of microgliosis [117], a harmful feedback loop potentiating neuroinflammation and neurotoxicity in SOD1^{G93A} mice could be established at the local level.

To determine whether axotomy potentiates the acquisition of a harmful microglial phenotype, the expression of CD68, Mac-2, and C1q was examined within Iba1-positive cells recruited around axotomized MN cell bodies. This analysis was performed in SOD1^{G93A} animals at presymptomatic (P60) and symptomatic (P90) stages and 7 days postaxotomy. Interestingly, at P60, the density of microglial cells with phagocytic activity, based on the CD68-expression analysis, was either unchanged or tended to be reduced as a consequence of axotomy. A similar result was observed when CD68 was evaluated in relation to mfSOD1 MN phenotypes. A comparable profile was found for Mac-2 expression as well. However, the opposite trend was observed at P90; at this age, the microglial neuroinflammatory response induced by axotomy entailed the acquisition of a worse microglial phenotype, which included the upregulation of CD68-positive particles and the acquisition of Mac-2 expression. Interestingly, C1q immunoreactivity was already induced on P60 by axotomy (Figure 11E–G).

The profile of microglial activation post axotomy in WT MNs is in some ways distinct because it does not entail the expression of Mac-2 [24].

4 | DISCUSSION

The availability of conformational-specific mfSOD1 antibodies allowed us to explore in detail the cellular distribution of these toxic SOD1 conformers and their association with MN degeneration and gliosis during ALS progression in SOD1^{G93A} mice. As targeting mutant SOD1 neurotoxicity is a significant approach for ALS therapy [42,47,118–120], the new information we provide here on the involvement of mfSOD1 in MN pathology may be relevant for future designs of SOD1-based ALS treatments. Most of our data on mfSOD1 localization were obtained using the C4F6 monoclonal antibody and are highly coincident with those previously reported using this antibody [39]. Additionally, according to animal species requirements, for multilabeling experiments, our rabbit anti-mfSOD1 AJ10 antibody was also applied when needed. Both antibodies yield the same pattern of immunoreactivity when analyzed together in spinal cord sections of SOD1^{G93A} mice [121]. We found that mfSOD1 immunoreactivity was primarily associated with MNs, starting on their dendritic and axonal expansions with a later accumulation on cell bodies. This sequential distribution allowed us to delimit, for operative purposes in this work, the three phenotypes described above. There was also a good correlation between the mfSOD1 signal and the presence of vacuoles in MNs. Vacuolar degeneration has been largely described in degenerating MNs in mutant SOD1 transgenic mouse models, with both mitochondria and ER as the primary organelles involved in vacuole formation [52–55,59,60,113,122]. Prominent mitochondrial swelling and vacuolization have also been observed in mice overexpressing human WT SOD1 in conjunction with other clinicopathological features shared by ALS [54].

As mitochondrial and/or ER dilatation are the hallmark features of paraptosis [61,62], we propose to apply this concept to vacuolated MNs in the context of mutant SOD1 ALS. Thus, extensive and emerging data regarding the molecular pathways involved in paraptotic cell death in a variety of contexts may eventually help to identify new targets for SOD1-mediated therapy in ALS. Vacuolated MN degeneration has also been observed during glutamate-mediated excitotoxic cell death and ER dilatation and fragmentation, which are also prominent ultrastructural features of this form of neuronal death [123,124]. However, mitochondrial swelling in this excitotoxic paradigm is not as massive as in ALS SOD1 MNs. Moreover, some degree of chromatin clumping, which we did not observe in ALS-SOD1 paraptotic-like MNs, is present in excitotoxic MNs.

Massive mitochondrial swelling in SOD1^{G93A} mice results from an expansion of the intermembrane space, in which the involvement of peroxisomes has been suggested as a membrane donor [53]. This form of mitochondrial swelling in SOD1^{G93A} mice is in contrast with the more common mechanism of pathological mitochondrial swelling that occurs by the increase in matrix volume because of altered ionic fluxes, osmotic imbalance, and opening of the permeability transition pore at the inner mitochondrial membranes [125]. This form of mitochondrial swelling is also seen in damaged cells present in the spinal cord of SOD1^{G93A} mice but coexists with prominent intermembrane swelling. Thus, mitochondrial damage in these mfSOD1-containing MNs seems to entail specific mechanisms and could be the consequence of a tissue-specific interaction of mutant SOD1 with molecular components of the surface of the outer mitochondrial membrane [52,126,127].

The ultrastructural appearance of the larger vacuoles (>5 μm diameter) suggests that they are formed by the fusion of some elementary units of already vacuolated mitochondria. As a consequence of the fusion of outer mitochondrial membranes, a single giant vacuole was formed. This giant vacuole contains several highly folded inner mitochondrial membrane complexes gathered at its peripheral wall, presumably originating after the fusion of several mitochondria carrying an extended outer membrane. It should be noted that large vacuolated spheroidal mitochondria, present in axons and dendrites simultaneously with mfSOD1 accumulation, are early events in SOD1^{G93A} MN pathology; this corresponds with the pattern designated the type 2 phenotype in this work, which is prominent at P30, long before the onset of symptoms. It is possible that the spatially restricted environmental conditions, characteristic of MN processes in relation to cell bodies, caused the mitochondria to present in axons and dendrites more vulnerable to mfSOD1 pathology. In this line, it has been shown that pathological elevations of neuronal Ca^{2+} start in dendrites and later propagate to somas [128]. Imbalanced intracellular Ca^{2+}, perturbations of ER-mitochondrial signaling, and protein misfolding are crucial elements determining paraptosis [61], which seems to be shared by mfSOD1-containing MNs.

In addition to mfSOD1 and mitochondrial proteins such as PDH, a large proportion of vacuoles contain other aberrantly localized proteins, such as Chrg, CD81, and flotillin, which are involved in the secretory pathway and EV biogenesis. The possible implications of these findings in the extracellular delivery of mutant SOD1 in conjunction with other proteins, as well as their involvement in the local spreading of ALS pathology, should be further analyzed. Other less abundant vacuolar inclusions that involve p62, PDH, and ubiquitin do not share mfSOD1 positivity and are likely related to mitophagy.

Alterations in the activity of afferent synaptic inputs may modulate the time course and severity of these early degenerative changes in mfSOD1-containing MNs. This

effect is consistent with our results detecting premature structural alterations in synaptic terminals contacting MNs and the observed effects of a pharmacological alteration of C-bouton-mediated neurotransmission. Our results demonstrated that treatment with methoctramine to block muscarinic cholinergic inputs results in a significant promotion of mfSOD1 expression in the ventral horn and changes the relative distribution of mfSOD1 MN phenotypes during ALS progression. This finding is consistent with data previously reported [15] and with the idea that hypoexcitability is a positive factor in the promotion of MN vulnerability in ALS [15,71,73,74,129,130]. It has been shown that the organization of postsynaptic glutamate receptors in synaptic afferents on MNs is critically disrupted before the alteration of their presynaptic partners in SOD1^{G93A} mice [71]. We observed early dismantling of the subsynaptic cistern associated with C-boutons, which presumably results in dysfunctional synaptic signaling in this particular type of synapse that critically regulates MN excitability [95]. As the normal organization of the ER appears severely disrupted in vacuolated MNs, it should be expected that the subsynaptic cistern, a specific ER subcompartment, may also be involved in this change. Thus, we must conclude that the decreased functionality of glutamatergic and cholinergic synapses contributes to MN hypoexcitability, mfSOD1 burden, and MN vacuolar degeneration.

Surprisingly, we found that paraptotic-like MNs exhibit positive immunoreactivity for flotillin and CD81 in their colocalization with PDH. Flotillin and CD81 are members of the tetraspanin family that regulate membrane morphology and dynamics, affecting intracellular trafficking, exocytosis-endocytosis, and intercellular signaling [131] that are also recognized as markers for EVs [65]. The identification of mitochondrial components in EVs displaying tetraspanin exosomal markers has been recently reported [68,132]. Thus, the existence of vacuoles containing mfSOD1 associated with tetraspanins and mitochondrial components in degenerating MNs indicates the possibility that they may be involved in the generation of EVs, which once released, contribute to local neuroinflammation and prion-like spreading of the disease [133–135]. Another possibility is that, once generated, vacuolated mitochondria may be disrupted as a consequence of a promotion of fission molecular mechanisms that seem to be activated in ALS [136]. Additionally, mitochondrial fragments may be eventually transferred to other neighboring cells [137,138].

Another novel aspect of vacuolated MNs is their content in pMLKL-positive particles, indicating activation of the terminal effector of necroptotic pathways. Using the same antibody, translocation of this protein from the cytosol to membrane fractions, including mitochondria, during necroptosis has been demonstrated. pMLKL-positive puncta have also been observed by immunofluorescence in cells undergoing necroptosis [67]. As, once

translocated, pMLKL is a membrane integrity disruptor, its role in the formation and release of mfSOD1-containing vesicles from vacuolated MNs should be further analyzed. Previous studies examining the involvement of necroptosis in ALS have reached unclear conclusions: necroptosis has been proposed as a mechanism for MN death induced by ALS astrocytes "in vitro" [139], and elevation of necroptotic markers, including MLKL, has been observed in spinal cords from SOD1^{G93A} mice and in patients with sporadic ALS [140]. However, the deletion of MLKL or either RIP1 or RIP3 kinases did not improve either the neuropathology or the clinical course of ALS in transgenic SOD1 mouse models [141–143]. In any case, the pathogenic role of necroptosis in ALS cannot be excluded because other pathogenic mechanisms may account for the lack of beneficial effects obtained by the deletion of necroptotic mediators in transgenic models [141]. In addition, we demonstrated here that other cell death mechanisms that could not be abolished in these mutants appear to be activated in nonvacuolated MNs during the advanced stages of the disease. Thus, the transient appearance of vacuolar degeneration on MNs and their necroptotic cell death in early stages of ALS can be envisaged as an "ignition point" from which a cascade of additional damaging pathways are induced in a progressive and devastating way.

Extracellular mfSOD1 does not kill MNs "per se", but when derived from neurons and astrocytes, it is a potent inducer of microglial activation and microglia-mediated neurotoxicity [64,117]. In agreement with our data, it has been shown that EVs of neuronal and astroglial origin may carry abundant mfSOD1 in SOD1-mediated ALS in humans and mouse models [135]. Neurosecretory proteins, such as chromogranins, interact with mutant SOD1 and mediate its secretion to the extracellular space, where it becomes indirectly toxic to MNs following microglial activation [64,117]. Our data on the coexistence of mfSOD1 with chromogranin, EV proteins (flotillin and CD81), and the membrane disruptor pMLKL in vacuolated MNs suggest that they might act as microglial attractors in the immediate vicinity of vacuolated MNs. For this reason, we topographically analyzed microglial recruitment in relation to the above-defined patterns of mfSOD1 expression in MNs. A good correlation between the severity of mfSOD1 accumulation in MNs and local microglial recruitment was observed among the distinct MN phenotypes (Figure 10). These locally positioned microglia display an activation profile with increased expression of CD68, Mac-2, and C1q, and vice versa, the status of microglia also impacts the extension of mfSOD1 accumulation and vacuolar degeneration of MNs. This assumption is supported by our experiments in which microgliosis was altered either by pharmacological elimination of microglia or by promoting Supplementary axotomy-induced chemotaxis and activation. This alteration indicates the crucial role of nonneuronal cells contributing to MN death via noncell-autonomous mechanisms [19].
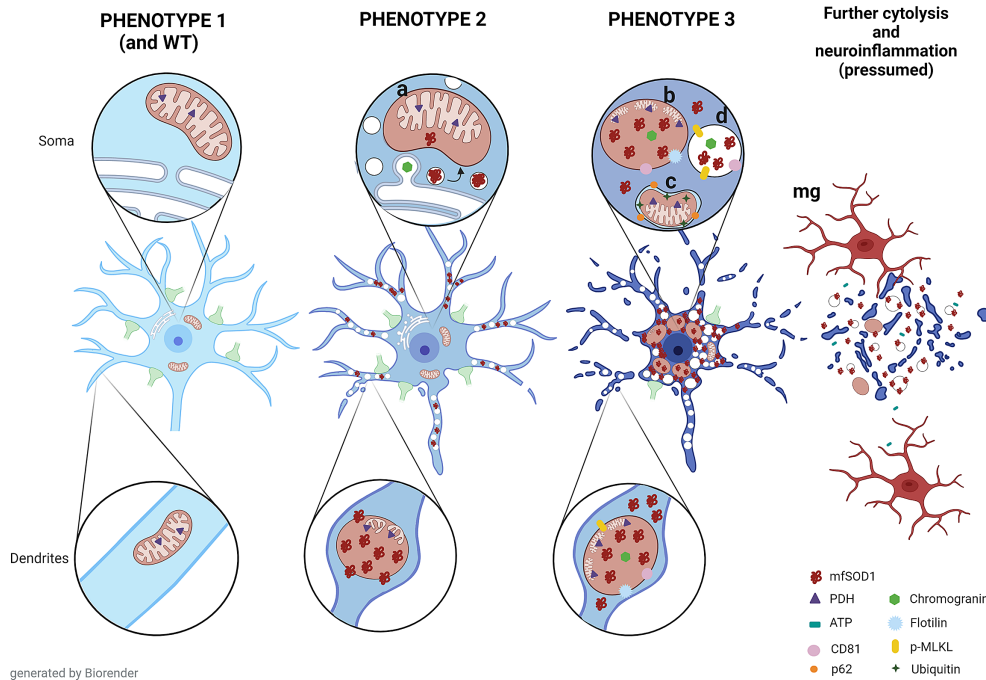
FIGURE 12 Schematic model of MN phenotypes described as a function of mfSOD1 expression and vacuolar degeneration. Phenotype 1 is similar to WT. in phenotype 2, mfSOD1 together with large mitochondrial vacuoles are abundant MN dendrites and axons but nearly absent in cell bodies. In MN somata, some ER-derived vesicles enriched in mfSOD1 accumulate and presumably fuse with mitochondria, producing an early expansion of their intermembranous space (a). In the type 3 phenotype, both MN cell bodies and processes are filled with vacuoles of heterogeneous size. Giant vacuoles result from the fusion of several mitochondria and ER vacuolar elements (b). In these vacuoles, mitochondrial and nonmitochondrial molecular components (PDH, Chrg, CD81, and flotillin) are shared in the same membrane-limited compartment. A minor proportion of vacuoles do not contain mfSOD1 but display positivity for p62, ubiquitin, and the mitochondrial marker PDH, indicating that they are mitophagic in nature (c). The necroptotic pathway is activated in MNs with the type 3 phenotype because pMLKL is present in some vacuoles (d). The end stage of the evolution of MNs with vacuolar degeneration involves their complete cytolysis with the release of mfSOD1-enriched vesicles to the extracellular space and the subsequent induction of a local neuroinflammatory response and the spreading of the disease (microglia, mg). Note the progressive loss of afferent synaptic inputs to MNs and the absence of chromatin condensation during the degenerative processes.

Microglia expressing mutant SOD1 are neurotoxic for MNs [99,117,144] and likely play a distinct pathogenic role according to the natural history of the disease. By eliminating the expression of mutant SOD1 in MNs, it was concluded that the protein is a primary determinant of disease onset, whereas decreasing mutant SOD1 levels in microglia slows disease progression [19]. Our data may fit with this concept if we consider that vacuolar MN degeneration, which predominates at the early presymptomatic stages, is followed by progressive glial activation and more extensive neurotoxicity triggered by the release of mfSOD1 and EVs from degenerating or disrupted vacuolar MNs. This second phase would be linked to the onset of paralysis and disease progression, in which microglial-derived neurotoxicity would affect the less vulnerable MN subtypes. Of note, according to our results and others [56], vacuolation is a transient process primarily affecting MMP9-positive fast-twitch, vulnerable MNs. We deduced that after disruption of MNs with increased ALS vulnerability, mfSOD1-mediated vacuolar degeneration does not involve the rest of the MN population that will undergo an ulterior degenerative pathology without a vacuolar phenotype.

Nonvacuolar MN degeneration develops in conjunction with a strong neuroinflammatory reaction involving astro- and microgliosis and with the progression of clinical symptoms. Thus, glial cell-mediated neurotoxicity may be particularly involved in these later mechanisms of MN degeneration, contrasting with the more cell-autonomous mutant SOD1-mediated vacuolar damage seen in earlier stages of the disease.

5 | CONCLUSIONS

Our results, which are summarized in Figure 12, more precisely map the neuropathological events occurring during the early and late stages of ALS progression in the SOD1^{G93A} mouse model. In particular, our attention was focused on the localization of mfSOD1 as a crucial determinant of the initial steps of MN degeneration, in which ER and mitochondrial vacuolation are the primary hallmarks. The association of mfSOD1-containing vacuoles with chromogranin, EV markers, and pMLKL indicates a new mechanism in which EVs derived from damaged MNs, via cellular secretion or necroptotic disruption, may be

triggers for the initial steps of neuroinflammation, glial-mediated neurotoxicity and disease spreading. More detailed knowledge of these processes, occurring long before the end stages of the disease, will allow us to identify novel molecular targets to be further investigated in future preclinical trials.

AUTHOR CONTRIBUTIONS

Josep E. Esquerda and SS conceived and designed the experiments. Sara Salvany, Anna Casanovas, Lídia Piedrafita, Sílvia Gras, and Josep E. Esquerda performed the acquisition, analysis, and interpretation of data. Josep E. Esquerda and Jordi Calderó wrote the manuscript.

CONFLICT OF INTEREST

SS, AC, LP, SG, JC, and JE have no competing interests concerning this study.

DATA AVAILABILITY STATEMENT

All the data and original images of this article are available upon reasonable request by e-mailing the corresponding author.

ORCID

Josep E. Esquerda https://orcid.org/0000-0003-1413-2103

REFERENCES

1. Rowland LP. Hereditary and acquired motor neuron diseases. City: Williams & Wilkins; 1995.
2. Rosen DR, Siddique T, Patterson D, Figlewicz DA, Sapp P, Hentati A, et al. Mutations in Cu/Zn superoxide dismutase gene are associated with familial amyotrophic lateral sclerosis. Nature. 1993;362:59–62. https://doi.org/10.1038/362059a0
3. Bruijn LI, Miller TM, Cleveland DW. Unraveling the mechanisms involved in motor neuron degeneration in ALS. Annu Rev Neurosci. 2004;27:723–49. https://doi.org/10.1146/annurev.neuro.27.070203.144244
4. Bendotti C, Carri MT. Lessons from models of SOD1-linked familial ALS. Trends Mol Med. 2004;10:393–400. https://doi.org/10.1016/j.molmed.2004.06.009
5. Ferraiuolo L, Kirby J, Grierson AJ, Sendtner M, Shaw PJ. Molecular pathways of motor neuron injury in amyotrophic lateral sclerosis. Nat Rev Neurol. 2011;7:616–30. https://doi.org/10.1038/nrneurol.2011.152
6. Gurney ME, Pu H, Chiu AY, Dal Canto MC, Polchow CY, Alexander DD, et al. Motor neuron degeneration in mice that express a human Cu,Zn superoxide dismutase mutation. Science. 1994;264:1772–5. https://doi.org/10.1126/science.8209258
7. Kato S. Amyotrophic lateral sclerosis models and human neuropathology: similarities and differences. Acta Neuropathol. 2008;115:97–114. https://doi.org/10.1007/s00401-007-0308-4
8. Turner BJ, Talbot K. Transgenics, toxicity and therapeutics in rodent models of mutant SOD1-mediated familial ALS. Prog Neurobiol. 2008;85:94–134. https://doi.org/10.1016/j.pneurobio.2008.01.001
9. Chiu AY, Zhai P, Dal Canto MC, Peters TM, Kwon YW, Prattis SM, et al. Age-dependent penetrance of disease in a transgenic mouse model of familial amyotrophic lateral sclerosis. Mol Cell Neurosci. 1995;6:349–62. https://doi.org/10.1006/mcne.1995.1027
10. Hall ED, Oostveen JA, Gurney ME. Relationship of microglial and astrocytic activation to disease onset and progression in a transgenic model of familial ALS. Glia. 1998;23:249–56. https://doi.org/10.1002/(sici)1098-1136(199807)23:3<249::aid-glia7>3.0.co;2-#
11. Hegedus J, Putman CT, Gordon T. Time course of preferential motor unit loss in the SOD1 G93A mouse model of amyotrophic lateral sclerosis. Neurobiol Dis. 2007;28:154–64. https://doi.org/10.1016/j.nbd.2007.07.003
12. Nijssen J, Comley LH, Hedlund E. Motor neuron vulnerability and resistance in amyotrophic lateral sclerosis. Acta Neuropathol. 2017;133:863–85. https://doi.org/10.1007/s00401-017-1708-8
13. Pun S, Santos AF, Saxena S, Xu L, Caroni P. Selective vulnerability and pruning of phasic motoneuron axons in motoneuron disease alleviated by CNTF. Nat Neurosci. 2006;9:408–19. https://doi.org/10.1038/nn1653
14. Kanning KC, Kaplan A, Henderson CE. Motor neuron diversity in development and disease. Annu Rev Neurosci. 2010;33:409–40. https://doi.org/10.1146/annurev.neuro.051508.135722
15. Saxena S, Roselli F, Singh K, Leptien K, Julien JP, Gros-Louis F, et al. Neuroprotection through excitability and mTOR required in ALS motoneurons to delay disease and extend survival. Neuron. 2013;80:80–96. https://doi.org/10.1016/j.neuron.2013.07.027
16. Lalancette-Hebert M, Sharma A, Lyashchenko AK, Shneider NA. Gamma motor neurons survive and exacerbate alpha motor neuron degeneration in ALS. Proc Natl Acad Sci USA. 2016;113:E8316–25. https://doi.org/10.1073/pnas.1605210113
17. Schaefer AM, Sanes JR, Lichtman JW. A compensatory subpopulation of motor neurons in a mouse model of amyotrophic lateral sclerosis. J Comp Neurol. 2005;490:209–19. https://doi.org/10.1002/cne.20620
18. Boillee S, Yamanaka K, Lobsiger CS, Copeland NG, Jenkins NA, Kassiotis G, et al. Onset and progression in inherited ALS determined by motor neurons and microglia. Science. 2006;312:1389–92. https://doi.org/10.1126/science.1123511
19. Clement AM, Nguyen MD, Roberts EA, Garcia ML, Boillee S, Rule M, et al. Wild-type nonneuronal cells extend survival of SOD1 mutant motor neurons in ALS mice. Science. 2003;302:113–7. https://doi.org/10.1126/science.1086071

20. Ilieva H, Polymenidou M, Cleveland DW. Non-cell autonomous toxicity in neurodegenerative disorders: ALS and beyond. J Cell Biol. 2009;187:761–72. https://doi.org/10.1083/jcb.200908164

21. Fischer LR, Culver DG, Tennant P, Davis AA, Wang MS, Castellano-Sanchez A, et al. Amyotrophic lateral sclerosis is a distal axonopathy: evidence in mice and man. Exp Neurol. 2004;185:232–40. https://doi.org/10.1016/j.expneurol.2003.10.004

22. Aldskogius H. Mechanisms and consequences of microglial responses to peripheral axotomy. Front Biosci. 2011;3:857–68. https://doi.org/10.2741/192

23. Rotterman TM, Alvarez FJ. Microglia dynamics and interactions with motoneurons axotomized after nerve injuries revealed by two-photon imaging. Sci Rep. 2020;10:8648. https://doi.org/10.1038/s41598-020-65363-9

24. Salvany S, Casanovas A, Piedrafita L, Tarabal O, Hernández S, Calderó J, et al. Microglial recruitment and mechanisms involved in the disruption of afferent synaptic terminals on spinal cord motor neurons after acute peripheral nerve injury. Glia. 2021;69:1216–40. https://doi.org/10.1002/glia.23959

25. Lowrie MB, Vrbová G. Dependence of postnatal motoneurones on their targets: review and hypothesis. Trends Neurosci. 1992;15:80–4. https://doi.org/10.1016/0166-2236(92)90014-y

26. Pollin MM, McHanwell S, Slater CR. The effect of age on motor neurone death following axotomy in the mouse. Development. 1991;112:83–9.

27. Rotterman TM, Akhter ET, Lane AR, MacPherson KP, Garcia VV, Tansey MG, et al. Spinal motor circuit synaptic plasticity after peripheral nerve injury depends on microglia activation and a CCR2 mechanism. J Neurosci. 2019;39:3412–33. https://doi.org/10.1523/JNEUROSCI.2945-17.2019

28. Oliveira AL, Thams S, Lidman O, Piehl F, Hokfelt T, Karre K, et al. A role for MHC class I molecules in synaptic plasticity and regeneration of neurons after axotomy. Proc Natl Acad Sci USA. 2004;101:17843–8. https://doi.org/10.1073/pnas.0408154101

29. Svensson M, Aldskogius H. Synaptic density of axotomized hypoglossal motorneurons following pharmacological blockade of the microglial cell proliferation. Exp Neurol. 1993;120:123–31. https://doi.org/10.1006/exnr.1993.1046

30. Ripps ME, Huntley GW, Hof PR, Morrison JH, Gordon JW. Transgenic mice expressing an altered murine superoxide dismutase gene provide an animal model of amyotrophic lateral sclerosis. Proc Natl Acad Sci USA. 1995;92:689–93. https://doi.org/10.1073/pnas.92.3.689

31. Mancuso R, Oliván S, Mancera P, Pastén-Zamorano A, Manzano R, Casas C, Osta R, Navarro X. Effect of genetic background on onset and disease progression in the SOD1-G93A model of amyotrophic lateral sclerosis. Amyotroph Lateral Scler. 2012;13:302–10. https://doi.org/10.3109/17482968.2012.662688

32. Günther R, Suhr M, Koch JC, Bähr M, Lingor P, Tönges L. Clinical testing and spinal cord removal in a mouse model for amyotrophic lateral sclerosis (ALS). J Vis Exp. 2012;(61):3936. https://doi.org/10.3791/3936

33. Burkholder T, Foltz C, Karlsson E, Linton CG, Smith JM. Health Evaluation of Experimental Laboratory Mice. Curr Protoc Mouse Biol. 2012;2:145–65. https://doi.org/10.1002/9780470942390.mo110217

34. Elmore MR, Najafi AR, Koike MA, Dagher NN, Spangenberg EE, Rice RA, et al. Colony-stimulating factor 1 receptor signaling is necessary for microglia viability, unmasking a microglia progenitor cell in the adult brain. Neuron. 2014;82:380–97. https://doi.org/10.1016/j.neuron.2014.02.040

35. Clarke PGH, Oppenheim RW. Neuron death in vertebrate development - in-vivo methods. Methods Cell Biol. 1995;46:277–321.

36. Watson C, Paxinos G, Kayalioglu G, Heise C. The spinal cord. City: Elsevier; 2009.

37. Rubio ME, Wenthold RJ. Differential distribution of intracellular glutamate receptors in dendrites. J Neurosci. 1999;19:5549–62. https://doi.org/10.1523/jneurosci.19-13-05549.1999

38. Bosco DA, Morfini G, Karabacak NM, Song Y, Gros-Louis F, Pasinelli P, et al. Wild-type and mutant SOD1 share an aberrant conformation and a common pathogenic pathway in ALS. Nat Neurosci. 2010;13:1396–403. https://doi.org/10.1038/nn.2660

39. Brotherton TE, Li Y, Cooper D, Gearing M, Julien JP, Rothstein JD, et al. Localization of a toxic form of superoxide dismutase 1 protein to pathologically affected tissues in familial ALS. Proc Natl Acad Sci USA. 2012;109:5505–10. https://doi.org/10.1073/pnas.1115009109

40. Fujisawa T, Homma K, Yamaguchi N, Kadowaki H, Tsuburaya N, Naguro I, et al. A novel monoclonal antibody reveals a conformational alteration shared by amyotrophic lateral sclerosis-linked SOD1 mutants. Ann Neurol. 2012;72:739–49. https://doi.org/10.1002/ana.23668

41. Hernández S, Casanovas A, Piedrafita L, Tarabal O, Esquerda JE. Neurotoxic species of misfolded SOD1G93A recognized by antibodies against the P2X4 subunit of the ATP receptor accumulate in damaged neurons of transgenic animal models of amyotrophic lateral sclerosis. J Neuropathol Exp Neurol. 2010;69:176–87. https://doi.org/10.1097/NEN.0b013e3181cd3e33

42. Maier M, Welt T, Wirth F, Montrasio F, Preisig D, McAfoose J, et al. A human-derived antibody targets misfolded SOD1 and ameliorates motor symptoms in mouse models of amyotrophic lateral sclerosis. Sci Transl Med. 2018;10. https://doi.org/10.1126/scitranslmed.aah3924

43. Pare B, Lehmann M, Beaudin M, Nordstrom U, Saikali S, Julien JP, et al. Misfolded SOD1 pathology in sporadic amyotrophic lateral sclerosis. Sci Rep. 2018;8:14223. https://doi.org/10.1038/s41598-018-31773-z

44. Pickles S, Vande Velde C. Misfolded SOD1 and ALS: zeroing in on mitochondria. Amyotroph Lateral Scler. 2012;13:333–40. https://doi.org/10.3109/17482968.2012.648645

45. Rakhit R, Robertson J, Vande Velde C, Horne P, Ruth DM, Griffin J, et al. An immunological epitope selective for pathological monomer-misfolded SOD1 in ALS. Nat Med. 2007;13:754–9. https://doi.org/10.1038/nm1559

46. Sábado J, Casanovas A, Hernandez S, Piedrafita L, Hereu M, Esquerda JE. Immunodetection of disease-associated conformers of mutant Cu/Zn superoxide dismutase 1 selectively expressed in degenerating neurons in amyotrophic lateral sclerosis. J Neuropathol Exp Neurol. 2013;72:646–61. https://doi.org/10.1097/NEN.0b013e318297fd10

47. Urushitani M, Ezzi SA, Julien JP. Therapeutic effects of immunization with mutant superoxide dismutase in mice models of amyotrophic lateral sclerosis. Proc Natl Acad Sci USA. 2007;104:2495–500. https://doi.org/10.1073/pnas.0606201104

48. Redler RL, Fee L, Fay JM, Caplow M, Dokholyan NV. Non-native soluble oligomers of Cu/Zn superoxide dismutase (SOD1) contain a conformational epitope linked to cytotoxicity in amyotrophic lateral sclerosis (ALS). Biochemistry. 2014;53:2423–32. https://doi.org/10.1021/bi500158w

49. Forsberg K, Jonsson PA, Andersen PM, Bergemalm D, Graffmo KS, Hultdin M, et al. Novel antibodies reveal inclusions containing non-native SOD1 in sporadic ALS patients. PLoS One. 2010;5:e11552. https://doi.org/10.1371/journal.pone.0011552

50. Rotunno MS, Bosco DA. An emerging role for misfolded wild-type SOD1 in sporadic ALS pathogenesis. Front Cell Neurosci. 2013;7:253. https://doi.org/10.3389/fncel.2013.00253

51. Liu J, Lillo C, Jonsson PA, Vande Velde C, Ward CM, Miller TM, et al. Toxicity of familial ALS-linked SOD1 mutants from selective recruitment to spinal mitochondria. Neuron. 2004;43:5–17. https://doi.org/10.1016/j.neuron.2004.06.016

52. Vande Velde C, Miller TM, Cashman NR, Cleveland DW. Selective association of misfolded ALS-linked mutant SOD1 with the cytoplasmic face of mitochondria. Proc Natl Acad Sci USA. 2008;105:4022–7. https://doi.org/10.1073/pnas.0712209105

53. Higgins CM, Jung C, Xu Z. ALS-associated mutant SOD1G93A causes mitochondrial vacuolation by expansion of the inter-membrane space and by involvement of SOD1 aggregation and peroxisomes. BMC Neurosci. 2003;4:16. https://doi.org/10.1186/1471-2202-4-16

54. Jaarsma D, Rognoni F, van Duijn W, Verspaget HW, Haasdijk ED, Holstege JC. CuZn superoxide dismutase (SOD1) accumulates in vacuolated mitochondria in transgenic mice expressing amyotrophic lateral sclerosis-linked SOD1 mutations. Acta Neuropathol. 2001;102:293–305. https://doi.org/10.1007/s004010100399

55. Wong PC, Pardo CA, Borchelt DR, Lee MK, Copeland NG, Jenkins NA, et al. An adverse property of a familial ALS-linked SOD1 mutation causes motor neuron disease characterized by vacuolar degeneration of mitochondria. Neuron. 1995;14:1105–16. https://doi.org/10.1016/0896-6273(95)90259-7

56. Kong J, Xu Z. Massive mitochondrial degeneration in motor neurons triggers the onset of amyotrophic lateral sclerosis in mice expressing a mutant SOD1. J Neurosci. 1998;18:3241–50. https://doi.org/10.1523/JNEUROSCI.18-09-03241.1998

57. Vinsant S, Mansfield C, Jimenez-Moreno R, Del Gaizo MV, Yoshikawa M, Hampton TG, et al. Characterization of early pathogenesis in the SOD1(G93A) mouse model of ALS: part I, background and methods. Brain Behav. 2013;3:335–50. https://doi.org/10.1002/brb3.143

58. Vinsant S, Mansfield C, Jimenez-Moreno R, Del Gaizo MV, Yoshikawa M, Hampton TG, et al. Characterization of early pathogenesis in the SOD1(G93A) mouse model of ALS: part II, results and discussion. Brain Behav. 2013;3:431–57. https://doi.org/10.1002/brb3.142

59. Bendotti C, Calvaresi N, Chiveri L, Prelle A, Moggio M, Braga M, et al. Early vacuolization and mitochondrial damage in motor neurons of FALS mice are not associated with apoptosis or with changes in cytochrome oxidase histochemical reactivity. J Neurol Sci. 2001;191:25–33. https://doi.org/10.1016/S0022-510x(01)00627-X

60. Martin LJ, Liu Z, Chen K, Price AC, Pan Y, Swaby JA, et al. Motor neuron degeneration in amyotrophic lateral sclerosis mutant superoxide dismutase-1 transgenic mice: mechanisms of mitochondriopathy and cell death. J Comp Neurol. 2007;500:20–46. https://doi.org/10.1002/cne.21160

61. Kim E, Lee DM, Seo MJ, Lee HJ, Choi KS. Intracellular Ca(2 +) imbalance critically contributes to paraptosis. Front Cell Dev Biol. 2020;8:607844. https://doi.org/10.3389/fcell.2020.607844

62. Sperandio S, de Belle I, Bredesen DE. An alternative, non-apoptotic form of programmed cell death. Proc Natl Acad Sci USA. 2000;97:14376–81. https://doi.org/10.1073/pnas.97.26.14376

63. Kaplan A, Spiller KJ, Towne C, Kanning KC, Choe GT, Geber A, et al. Neuronal matrix metalloproteinase-9 is a determinant of selective neurodegeneration. Neuron. 2014;81:333–48. https://doi.org/10.1016/j.neuron.2013.12.009

64. Urushitani M, Sik A, Sakurai T, Nukina N, Takahashi R, Julien JP. Chromogranin-mediated secretion of mutant superoxide dismutase proteins linked to amyotrophic lateral sclerosis. Nat Neurosci. 2006;9:108–18. https://doi.org/10.1038/nn1603

65. Kowal J, Arras G, Colombo M, Jouve M, Morath JP, Primdal-Bengtson B, et al. Proteomic comparison defines novel markers to characterize heterogeneous populations of extracellular vesicle subtypes. Proc Natl Acad Sci USA. 2016;113:E968–77. https://doi.org/10.1073/pnas.1521230113

66. Vilcaes AA, Chanaday NL, Kavalali ET. Interneuronal exchange and functional integration of synaptobrevin via extracellular vesicles. Neuron. 2021;109:971–983.e975. https://doi.org/10.1016/j.neuron.2021.01.007

67. Wang H, Sun L, Su L, Rizo J, Liu L, Wang LF, et al. Mixed lineage kinase domain-like protein MLKL causes necrotic membrane disruption upon phosphorylation by RIP3. Mol Cell. 2014;54:133–46. https://doi.org/10.1016/j.molcel.2014.03.003

68. D'Acunzo P, Perez-Gonzalez R, Kim Y, Hargash T, Miller C, Alldred MJ, et al. Mitovesicles are a novel population of extracellular vesicles of mitochondrial origin altered in Down syndrome. Sci Adv. 2021;7. https://doi.org/10.1126/sciadv.abe5085

69. Rudnick ND, Griffey CJ, Guarnieri P, Gerbino V, Wang X, Piersaint JA, et al. Distinct roles for motor neuron autophagy early and late in the SOD1(G93A) mouse model of ALS. Proc Natl Acad Sci USA. 2017;114:E8294–303. https://doi.org/10.1073/pnas.1704294114

70. Yamada T, Dawson TM, Yanagawa T, Iijima M, Sesaki H. SQSTM1/p62 promotes mitochondrial ubiquitination independently of PINK1 and PRKN/parkin in mitophagy. Autophagy. 2019;15:2012–8. https://doi.org/10.1080/15548627.2019.1643185

71. Baczyk M, Alami NO, Delestree N, Martinot C, Tang L, Commisso B, et al. Synaptic restoration by cAMP/PKA drives activity-dependent neuroprotection to motoneurons in ALS. J Exp Med. 2020;217. https://doi.org/10.1084/jem.20191734

72. Chang Q, Martin LJ. Glycinergic innervation of motoneurons is deficient in amyotrophic lateral sclerosis mice a quantitative confocal analysis. Am J Pathol. 2009;174:574–85. https://doi.org/10.2353/ajpath.2009.080557

73. Delestrée N, Manuel M, Iglesias C, Elbasiouny SM, Heckman CJ, Zytnicki D. Adult spinal motoneurones are not hyperexcitable in a mouse model of inherited amyotrophic lateral sclerosis. J Physiol. 2014;592:1687–703. https://doi.org/10.1113/jphysiol.2013.265843

74. Martinez-Silva ML, Imhoff-Manuel RD, Sharma A, Heckman CJ, Shneider NA, Roselli F, et al. Hypoexcitability precedes denervation in the large fast-contracting motor units in two unrelated mouse models of ALS. Elife. 2018;7. https://doi.org/10.7554/eLife.30955

75. Roselli F, Caroni P. From intrinsic firing properties to selective neuronal vulnerability in neurodegenerative diseases. Neuron. 2015;85:901–10. https://doi.org/10.1016/j.neuron.2014.12.063

76. Schutz B. Imbalanced excitatory to inhibitory synaptic input precedes motor neuron degeneration in an animal model of amyotrophic lateral sclerosis. Neurobiol Dis. 2005;20:131–40. https://doi.org/10.1016/j.nbd.2005.02.006

77. Zang DW, Lopes EC, Cheema SS. Loss of synaptophysin-positive boutons on lumbar motor neurons innervating the medial gastrocnemius muscle of the SOD1G93A G1H transgenic mouse model of ALS. J Neurosci Res. 2005;79:694–9. https://doi.org/10.1002/jnr.20379

78. Zhao P, Ignacio S, Beattie EC, Abood ME. Altered presymptomatic AMPA and cannabinoid receptor trafficking in motor neurons of ALS model mice: implications for excitotoxicity. Eur J Neurosci. 2008;27:572–9. https://doi.org/10.1111/j.1460-9568.2008.06041.x

79. Conradi S, Kellerth JO, Berthold CH. Electron microscopic studies of serially sectioned cat spinal alpha-motoneurons. II. A method for the description of architecture and synaptology of the cell body and proximal dendritic segments. J Comp Neurol. 1979;184:741–54. https://doi.org/10.1002/cne.901840407

80. Christensen BN. Morphological correlates of synaptic transmission in lamprey spinal cord. J Neurophysiol. 1976;39:197–212. https://doi.org/10.1152/jn.1976.39.2.197

81. Haimann C, Torri-Tarelli F, Fesce R, Ceccarelli B. Measurement of quantal secretion induced by ouabain and its correlation with depletion of synaptic vesicles. J Cell Biol. 1985;101:1953–65. https://doi.org/10.1083/jcb.101.5.1953

82. Heuser JE, Reese TS. Evidence for recycling of synaptic vesicle membrane during transmitter release at the frog neuromuscular junction. J Cell Biol. 1973;57:315–44. https://doi.org/10.1083/jcb.57.2.315

83. Soykan T, Kaempf N, Sakaba T, Vollweiter D, Goerdeler F, Puchkov D, et al. Synaptic vesicle endocytosis occurs on multiple timescales and is mediated by formin-dependent actin assembly. Neuron. 2017;93:854–866.e854. https://doi.org/10.1016/j.neuron.2017.02.011

84. Miles GB, Hartley R, Todd AJ, Brownstone RM. Spinal cholinergic interneurons regulate the excitability of motoneurons during locomotion. Proc Natl Acad Sci USA. 2007;104:2448–53. https://doi.org/10.1073/pnas.0611134104

85. Dukkipati SS, Chihi A, Wang Y, Elbasiouny SM. Experimental design and data analysis issues contribute to inconsistent results of C-bouton changes in amyotrophic lateral sclerosis. eNeuro. 2017;4:ENEURO.0281-16.2016. https://doi.org/10.1523/ENEURO.0281-16.2016

86. Casas C, Herrando-Grabulosa M, Manzano R, Mancuso R, Osta R, Navarro X. Early presymptomatic cholinergic dysfunction in a murine model of amyotrophic lateral sclerosis. Brain Behav. 2013;3:145–58. https://doi.org/10.1002/brb3.104

87. Herron LR, Miles GB. Gender-specific perturbations in modulatory inputs to motoneurons in a mouse model of amyotrophic lateral sclerosis. Neuroscience. 2012;226:313–23. https://doi.org/10.1016/j.neuroscience.2012.09.031

88. Lasiene J, Komine O, Fujimori-Tonou N, Powers B, Endo F, Watanabe S, et al. Neuregulin 1 confers neuroprotection in SOD1-linked amyotrophic lateral sclerosis mice via restoration of C-boutons of spinal motor neurons. Acta Neuropathol Commun. 2016;4:15. https://doi.org/10.1186/s40478-016-0286-7

89. Milan L, Courtand G, Cardoit L, Masmejean F, Barriere G, Cazalets JR, et al. Age-related changes in pre- and postsynaptic partners of the cholinergic C-boutons in wild-type and SOD1G93A lumbar motoneurons. PLoS One. 2015;10:e0135525. https://doi.org/10.1371/journal.pone.0135525

90. Nagao M, Misawa H, Kato S, Hirai S. Loss of cholinergic synapses on the spinal motor neurons of amyotrophic lateral sclerosis. J Neuropathol Exp Neurol. 1998;57:329–33. https://doi.org/10.1097/00005072-199804000-00004

91. Pullen AH, Athanasiou D. Increase in presynaptic territory of C-terminals on lumbar motoneurons of G93A SOD1 mice during disease progression. Eur J Neurosci. 2009;29:551–61. https://doi.org/10.1111/j.1460-9568.2008.06602.x

92. Casanovas A, Salvany S, Lahoz V, Tarabal O, Piedrafita L, Sabater R, et al. Neuregulin 1-ErbB module in C-bouton synapses on somatic motor neurons: molecular compartmentation and response to peripheral nerve injury. Sci Rep. 2017;7:40155. https://doi.org/10.1038/srep40155

93. Gallart-Palau X, Tarabal O, Casanovas A, Sabado J, Correa FJ, Hereu M, et al. Neuregulin-1 is concentrated in the postsynaptic subsurface cistern of C-bouton inputs to alpha-motoneurons and altered during motoneuron diseases. FASEB J. 2014;28:3618–32. https://doi.org/10.1096/fj.13-248583

94. Deardorff AS, Romer SH, Fyffe REW. Location, location, location: the organization and roles of potassium channels in mammalian motoneurons. J Physiol. 2021;599:1391–420. https://doi.org/10.1113/JP278675

95. Witts EC, Zagoraiou L, Miles GB. Anatomy and function of cholinergic C bouton inputs to motor neurons. J Anat. 2014;224:52–60. https://doi.org/10.1111/joa.12063

96. Beers DR, Zhao W, Liao B, Kano O, Wang J, Huang A, et al. Neuroinflammation modulates distinct regional and temporal clinical responses in ALS mice. Brain Behav Immun. 2011;25:1025–35. https://doi.org/10.1016/j.bbi.2010.12.008

97. Clarke BE, Patani R. The microglial component of amyotrophic lateral sclerosis. Brain. 2020;143:3526–39. https://doi.org/10.1093/brain/awaa309

98. D'Erchia AM, Gallo A, Manzari C, Raho S, Horner DS, Chiara M, et al. Massive transcriptome sequencing of human spinal cord tissues provides new insights into motor neuron degeneration in ALS. Sci Rep. 2017;7. Artn 1004610.1038/S41598-017-10488-7

99. Frakes AE, Ferraiuolo L, Haidet-Phillips AM, Schmelzer L, Braun L, Miranda CJ, et al. Microglia induce motor neuron death via the classical NF-kappaB pathway in amyotrophic lateral sclerosis. Neuron. 2014;81:1009–23. https://doi.org/10.1016/j.neuron.2014.01.013

100. Nagai M, Re DB, Nagata T, Chalazonitis A, Jessell TM, Wichterle H, et al. Astrocytes expressing ALS-linked mutated SOD1 release factors selectively toxic to motor neurons. Nat Neurosci. 2007;10:615–22. https://doi.org/10.1038/nn1876

101. Philips T, Robberecht W. Neuroinflammation in amyotrophic lateral sclerosis: role of glial activation in motor neuron disease. Lancet Neurol. 2011;10:253–63. https://doi.org/10.1016/S1474-4422(11)70015-1

102. Geloso MC, Corvino V, Marchese E, Serrano A, Michetti F, D'Ambrosi N. The dual role of microglia in ALS: mechanisms and therapeutic approaches. Front Aging Neurosci. 2017;9:242. https://doi.org/10.3389/fnagi.2017.00242

103. Zhao W, Beers DR, Appel SH. Immune-mediated mechanisms in the pathoprogression of amyotrophic lateral sclerosis. J Neuroimmune Pharmacol. 2013;8:888–99. https://doi.org/10.1007/s11481-013-9489-x

104. Maniatis S, Aijo T, Vickovic S, Braine C, Kang K, Mollbrink A, et al. Spatiotemporal dynamics of molecular pathology in amyotrophic lateral sclerosis. Science. 2019;364:89–93. https://doi.org/10.1126/science.aav9776

105. Sanagi T, Yuasa S, Nakamura Y, Suzuki E, Aoki M, Warita H, et al. Appearance of phagocytic microglia adjacent to motoneurons in spinal cord tissue from a presymptomatic transgenic rat model of amyotrophic lateral sclerosis. J Neurosci Res. 2010;88:2736–46. https://doi.org/10.1002/jnr.22424

106. Reichert F, Rotshenker S. Galectin-3 (MAC-2) controls microglia phenotype whether amoeboid and phagocytic or branched and non-phagocytic by regulating the cytoskeleton. Front Cell Neurosci. 2019;13:90. https://doi.org/10.3389/fncel.2019.00090

107. Sasaki Y, Hoshi M, Akazawa C, Nakamura Y, Tsuzuki H, Inoue K, et al. Selective expression of Gi/o-coupled ATP receptor P2Y12 in microglia in rat brain. Glia. 2003;44:242–50. https://doi.org/10.1002/glia.10293

108. Haynes SE, Hollopeter G, Yang G, Kurpius D, Dailey ME, Gan WB, et al. The P2Y12 receptor regulates microglial activation by extracellular nucleotides. Nat Neurosci. 2006;9:1512–9. https://doi.org/10.1038/nn1805

109. Dadon-Nachum M, Melamed E, Offen D. The "dying-back" phenomenon of motor neurons in ALS. J Mol Neurosci. 2011;43:470–7. https://doi.org/10.1007/s12031-010-9467-1

110. Mariotti R, Cristino L, Bressan C, Boscolo S, Bentivoglio M. Altered reaction of facial motoneurons to axonal damage in the presymptomatic phase of a murine model of familial amyotrophic lateral sclerosis. Neuroscience. 2002;115:331–5. https://doi.org/10.1016/s0306-4522(02)00448-7

111. Schram S, Chuang D, Schmidt G, Piponov H, Helder C, Kerns J, et al. Mutant SOD1 prevents normal functional recovery through enhanced glial activation and loss of motor neuron innervation after peripheral nerve injury. Neurobiol Dis. 2019;124:469–78. https://doi.org/10.1016/j.nbd.2018.12.020

112. Sharp PS, Dick JR, Greensmith L. The effect of peripheral nerve injury on disease progression in the SOD1(G93A) mouse model of amyotrophic lateral sclerosis. Neuroscience. 2005;130:897–910. https://doi.org/10.1016/j.neuroscience.2004.09.069

113. Kong J, Xu Z. Peripheral axotomy slows motoneuron degeneration in a transgenic mouse line expressing mutant SOD1 G93A. J Comp Neurol. 1999;412:373–80. https://doi.org/10.1002/(sici)1096-9861(19990920)412:2<373::aid-cne13>3.0.co;2-n

114. Sharp PS, Tyreman N, Jones KE, Gordon T. Crush injury to motor nerves in the G93A transgenic mouse model of amyotrophic lateral sclerosis promotes muscle reinnervation and survival of functionally intact nerve-muscle contacts. Neurobiol Dis. 2018;113:33–44. https://doi.org/10.1016/j.nbd.2018.01.019

115. Salvany S, Casanovas A, Tarabal O, Piedrafita L, Hernandez S, Santafe M, et al. Localization and dynamic changes of neuregulin-1 at C-type synaptic boutons in association with motor neuron injury and repair. FASEB J. 2019;33:7833–51. https://doi.org/10.1096/fj.201802329R

116. Beers DR, Henkel JS, Xiao Q, Zhao W, Wang J, Yen AA, et al. Wild-type microglia extend survival in PU.1 knockout mice with

familial amyotrophic lateral sclerosis. Proc Natl Acad Sci USA. 2006;103:16021–6. https://doi.org/10.1073/pnas.0607423103

117. Zhao W, Beers DR, Henkel JS, Zhang W, Urushitani M, Julien JP, et al. Extracellular mutant SOD1 induces microglial-mediated motoneuron injury. Glia. 2010;58:231–43. https://doi.org/10.1002/glia.20919

118. Gros-Louis F, Soucy G, Lariviere R, Julien JP. Intra-cerebroventricular infusion of monoclonal antibody or its derived Fab fragment against misfolded forms of SOD1 mutant delays mortality in a mouse model of ALS. J Neurochem. 2010;113: 1188–99. https://doi.org/10.1111/j.1471-4159.2010.06683.x

119. Liu HN, Tjostheim S, Dasilva K, Taylor D, Zhao B, Rakhit R, et al. Targeting of monomer/misfolded SOD1 as a therapeutic strategy for amyotrophic lateral sclerosis. J Neurosci. 2012;32: 8791–9. https://doi.org/10.1523/JNEUROSCI.5053-11.2012

120. Raoul C, Abbas-Terki T, Bensadoun JC, Guillot S, Haase G, Szulc J, et al. Lentiviral-mediated silencing of SOD1 through RNA interference retards disease onset and progression in a mouse model of ALS. Nat Med. 2005;11:423–8. https://doi.org/10.1038/nm1207

121. Sabado J, Casanovas A, Rodrigo H, Arque G, Esquerda JE. Adverse effects of a SOD1-peptide immunotherapy on SOD1 G93A mouse slow model of amyotrophic lateral sclerosis. Neuroscience. 2015;310:38–50. https://doi.org/10.1016/j.neuroscience.2015.09.027

122. Dal Canto MC, Gurney ME. Development of central nervous system pathology in a murine transgenic model of human amyotrophic lateral sclerosis. Am J Pathol. 1994;145:1271–9.

123. Calderó J, Ciutat D, Lladó J, Castán E, Oppenheim RW, Esquerda JE. Effects of excitatory amino acids on neuromuscular development in the chick embryo. J Comp Neurol. 1997;387:73–95.

124. Ishimaru MJ, Ikonomidou C, Tenkova TI, Der TC, Dikranian K, Sesma MA, et al. Distinguishing excitotoxic from apoptotic neurodegeneration in the developing rat brain. J Comp Neurol. 1999; 408:461–76.

125. Javadov S, Chapa-Dubocq X, Makarov V. Different approaches to modeling analysis of mitochondrial swelling. Mitochondrion. 2018;38:58–70. https://doi.org/10.1016/j.mito.2017.08.004

126. Israelson A, Arbel N, Da Cruz S, Ilieva H, Yamanaka K, Shoshan-Barmatz V, et al. Misfolded mutant SOD1 directly inhibits VDAC1 conductance in a mouse model of inherited ALS. Neuron. 2010;67: 575–87. https://doi.org/10.1016/j.neuron.2010.07.019

127. Pedrini S, Sau D, Guareschi S, Bogush M, Brown RH Jr, Naniche N, et al. ALS-linked mutant SOD1 damages mitochondria by promoting conformational changes in Bcl-2. Hum Mol Genet. 2010;19:2974–86. https://doi.org/10.1093/hmg/ddq202

128. Vander Jagt TA, Connor JA, Shuttleworth CW. Localized loss of Ca^{2+} homeostasis in neuronal dendrites is a downstream consequence of metabolic compromise during extended NMDA exposures. J Neurosci. 2008;28:5029–39. https://doi.org/10.1523/JNEUROSCI.5069-07.2008

129. Filipchuk A, Pambo-Pambo A, Gaudel F, Liabeuf S, Brocard C, Gueritaud JP, et al. Early hypoexcitability in a subgroup of spinal motoneurons in superoxide dismutase 1 transgenic mice, a model of amyotrophic lateral sclerosis. Neuroscience. 2021;463:337–53. https://doi.org/10.1016/j.neuroscience.2021.01.039

130. Ruegsegger C, Maharjan N, Goswami A, Filezac de L'Etang A, Weis J, Troost D, et al. Aberrant association of misfolded SOD1 with Na(+)/K(+)ATPase-alpha3 impairs its activity and contributes to motor neuron vulnerability in ALS. Acta Neuropathol. 2016;131:427–51. https://doi.org/10.1007/s00401-015-1510-4

131. Hemler ME. Tetraspanin functions and associated microdomains. Nat Rev Mol Cell Biol. 2005;6:801–11. https://doi.org/10.1038/nrm1736

132. Picca A, Beli R, Calvani R, Coelho-Junior HJ, Landi F, Bernabei R, et al. Older adults with physical frailty and sarcopenia show increased levels of circulating small extracellular vesicles with a specific mitochondrial signature. Cell. 2020;9. https://doi.org/10.3390/cells9040973

133. Bellingham SA, Guo BB, Coleman BM, Hill AF. Exosomes: vehicles for the transfer of toxic proteins associated with neurodegenerative diseases? Front Physiol. 2012;3:124. https://doi.org/10.3389/fphys.2012.00124

134. Grad LI, Yerbury JJ, Turner BJ, Guest WC, Pokrishevsky E, O'Neill MA, et al. Intercellular propagated misfolding of wild-type Cu/Zn superoxide dismutase occurs via exosome-dependent and -independent mechanisms. Proc Natl Acad Sci USA. 2014;111: 3620–5. https://doi.org/10.1073/pnas.1312245111

135. Silverman JM, Christy D, Shyu CC, Moon KM, Fernando S, Gidden Z, et al. CNS-derived extracellular vesicles from superoxide dismutase 1 (SOD1)(G93A) ALS mice originate from astrocytes and neurons and carry misfolded SOD1. J Biol Chem. 2019; 294:3744–59. https://doi.org/10.1074/jbc.RA118.004825

136. Joshi AU, Saw NL, Vogel H, Cunningham AD, Shamloo M, Mochly-Rosen D. Inhibition of Drp1/Fis1 interaction slows progression of amyotrophic lateral sclerosis. EMBO Mol Med. 2018; 10. https://doi.org/10.15252/emmm.201708166

137. Hayakawa K, Esposito E, Wang X, Terasaki Y, Liu Y, Xing C, et al. Transfer of mitochondria from astrocytes to neurons after stroke. Nature. 2016;535:551–5. https://doi.org/10.1038/nature18928

138. Joshi AU, Minhas PS, Liddelow SA, Haileselassie B, Andreasson KI, Dorn GW II, et al. Fragmented mitochondria released from microglia trigger A1 astrocytic response and propagate inflammatory neurodegeneration. Nat Neurosci. 2019;22: 1635–48. https://doi.org/10.1038/s41593-019-0486-0

139. Re DB, Le Verche V, Yu C, Amoroso MW, Politi KA, Phani S, et al. Necroptosis drives motor neuron death in models of both sporadic and familial ALS. Neuron. 2014;81:1001–8. https://doi.org/10.1016/j.neuron.2014.01.011

140. Ito Y, Ofengeim D, Najafov A, Das S, Saberi S, Li Y, et al. RIPK1 mediates axonal degeneration by promoting inflammation and necroptosis in ALS. Science. 2016;353:603–8. https://doi.org/10.1126/science.aaf6803

141. Dermentzaki G, Politi KA, Lu L, Mishra V, Pérez-Torres EJ, Sosunov AA, et al. Deletion of Ripk3 prevents motor neuron death in vitro but not in vivo. eNeuro. 2019;6:ENEURO.0308-18.2018. https://doi.org/10.1523/ENEURO.0308-18.2018

142. Dominguez S, Varfolomeev E, Brendza R, Stark K, Tea J, Imperio J, et al. Genetic inactivation of RIP1 kinase does not ameliorate disease in a mouse model of ALS. Cell Death Differ. 2021; 28:915–31. https://doi.org/10.1038/s41418-020-00625-7

143. Wang T, Perera ND, Chiam MDF, Cuic B, Wanniarachchillage N, Tomas D, et al. Necroptosis is dispensable for motor neuron degeneration in a mouse model of ALS. Cell Death Differ. 2020;27:1728–39. https://doi.org/10.1038/s41418-019-0457-8

144. Xiao Q, Zhao W, Beers DR, Yen AA, Xie W, Henkel JS, et al. Mutant SOD1(G93A) microglia are more neurotoxic relative to wild-type microglia. J Neurochem. 2007;102:2008–19. https://doi.org/10.1111/j.1471-4159.2007.04677.x

SUPPORTING INFORMATION

Additional supporting information may be found in the online version of the article at the publisher's website.